การวัดค่าประสิทธิภาพเชิงควอนตัมของเซลล์สุริยะ $CuIn_{1-x}Ga_xSe_2$

นายสุภทัต สุขเอี่ยม

วิทยานิพนธ์นี้เป็นส่วนหนึ่งของการศึกษาตามหลักสูตรปริญญาวิทยาศาสตรมหาบัณฑิต
สาขาวิชาฟิสิกส์ ภาควิชาฟิสิกส์
คณะวิทยาศาสตร์ จุฬาลงกรณ์มหาวิทยาลัย
ปีการศึกษา 2557

QUANTUM EFFICIENCY MEASUREMENTS OF $CuIn_{1-x}Ga_xSe_2$ SOLAR CELLS

Mr. Supathat Sukaiem

A Thesis Submitted in Partial Fulfillment of the Requirements
for the Degree of Master of Science Program in Physics
Department of Physics
Faculty of Science
Chulalongkorn University
Academic Year 2014

Thesis Title	QUANTUM EFFICIENCY MEASUREMENTS OF $CuIn_{1-x}Ga_xSe_2$ SOLAR CELLS
By	Mr. Supathat Sukaiem
Field of Study	Physics
Thesis Advisor	Assistant Professor Sojiphong Chatraphorn, Ph.D.

Accepted by the Faculty of Science, Chulalongkorn University in Partial Fulfillment of the Requirements for the Master's Degree

.....Dean of the Faculty of Science
(Professor Supot Hannongbua, Dr.rer.nat.)

THESIS COMMITTEE

.....Chairman
(Assistant Professor Rattachat Mongkolnavin, Ph.D.)
.....Thesis Advisor
(Assistant Professor Sojiphong Chatraphorn, Ph.D.)
.....Examiner
(Assistant Professor Tonphong Kaewkongka, Ph.D.)
.....External Examiner
(Rachsak Sakdanuphab, Ph.D.)

สุภทัต สุขเอี่ยม : การวัดค่าประสิทธิภาพเชิงควอนตัมของเซลล์สุริยะ $CuIn_{1-x}Ga_xSe_2$ (QUANTUM EFFICIENCY MEASUREMENTS OF $CuIn_{1-x}Ga_xSe_2$ SOLAR CELLS) อ.ที่ปรึกษาวิทยานิพนธ์หลัก: ผศ. ดร. โศจิพงศ์ ฉัตราภรณ์, 63 หน้า.

การวัดค่าประสิทธิภาพเชิงควอนตัมเป็นหนึ่งในวิธีการที่ใช้สำหรับทดสอบการทำงานของเซลล์สุริยะโดยเฉพาะอย่างยิ่งในด้านของการกักเก็บพาหะตัวนำไฟฟ้า ค่าประสิทธิภาพเชิงควอนตัมบ่งบอกถึงจำนวนของกระแสไฟฟ้าที่ถูกผลิตขึ้นเมื่อเซลล์สุริยะได้รับการฉายแสงด้วยความยาวคลื่นค่าหนึ่งๆ ในการศึกษานี้ระบบการวัดค่าประสิทธิภาพเชิงควอนตัมได้ถูกสร้างขึ้นและถูกนำมาใช้วิเคราะห์เซลล์สุริยะชนิดฟิล์มบาง $CuIn_{1-x}Ga_xSe_2$ หรือ CIGS ที่มีเงื่อนไขการปลูกที่แตกต่างกัน ผลของค่าประสิทธิภาพเชิงควอนตัมได้แสดงให้เห็นถึงอิทธิพลของความแตกต่างของช่องว่างแถบพลังงานที่มีต่อการกักเก็บกระแสไฟฟ้า และยังแสดงให้เห็นถึงการเปลี่ยนแปลงของจำนวนกระแสไฟฟ้าที่กักเก็บได้โดยรวมและขอบเขตการดูดกลืนแสงของเซลล์สุริยะอีกด้วย นอกจากนี้การวัดค่าประสิทธิภาพเชิงควอนตัมยังถูกนำไปใช้ระบุสมบัติทางไฟฟ้าของฟิล์มบางแต่ละชั้นที่ประกอบกันเป็นเซลล์สุริยะได้ โดยที่การสูญเสียกระแสไฟฟ้าจากการรั่วไหล ณ บริเวณรอยต่อ พี-เอ็น ที่ไม่สมบูรณ์จะนำไปสู่การตกอย่างฉับพลันปรากฏขึ้นที่ความยาวคลื่นบางค่าในผลของค่าประสิทธิภาพเชิงควอนตัม อย่างไรก็ตาม ไม่เพียงแค่เทคนิควิธีพื้นฐานได้ถูกใช้ในการวัดค่าประสิทธิภาพเชิงควอนตัม แต่เทคนิคล็อกอินก็ยังถูกประยุกต์ใช้กับระบบนี้เพื่อเพิ่มอัตราส่วนระหว่างสัญญาณที่ต้องการวัดต่อสัญญาณรบกวนอื่นๆ ผลจากการเปรียบเทียบของทั้งสองวิธีข้างต้นได้แสดงให้เห็นถึงการปรับปรุงให้ดีขึ้นในด้านการเก็บข้อมูลการทดลอง ทำให้ระบบมีความน่าเชื่อถือมากขึ้น และการศึกษาท้ายสุดที่เกี่ยวข้องกับการไบแอสความต่างศักย์แก่เซลล์สุริยะเพื่อทดสอบการทำงานที่เงื่อนไขใกล้เคียงกับการใช้งานจริงมากขึ้น พบว่าผลจากความกว้างของเขตปลอดพาหะที่แคบลงทำให้ความสามารถในการกักเก็บกระแสของเซลล์สุริยะในเงื่อนไขดังกล่าวลดลงตามไปด้วย

ภาควิชา ฟิสิกส์ ลายมือชื่อนิสิต .....

สาขาวิชา ฟิสิกส์ ลายมือชื่อ อ.ที่ปรึกษาหลัก .....

ปีการศึกษา 2557

5572153023 : MAJOR PHYSICS
KEYWORDS: QUANTUM EFFICIENCY / CIGS / PHOTORESPONSE / PHOTOCURRENT

SUPATHAT SUKAIEM: QUANTUM EFFICIENCY MEASUREMENTS OF $CuIn_{1-x}Ga_xSe_2$ SOLAR CELLS. ADVISOR: ASST. PROF. SOJIPHONG CHATRAPHORN, Ph.D., 63 pp.

Quantum efficiency (QE) measurement is one of several methods used to investigate solar cell performance, especially the carrier collection. It indicates the amount of photogenerated current produced when a solar cell is illuminated by photons of a particular wavelength. In this study, a quantum efficiency measurement system was constructed and the $CuIn_{1-x}Ga_xSe_2$ (CIGS) – based thin film solar cells with different growth conditions were characterized. The results show an influence of differences in band gap energy on photo-current collection. The changing in collected current and absorption edges can be observed. In addition, quantum efficiency measurement is used to identify the properties of each thin film layer comprising the devices. The current leakage due to a defective p-n junction leads to abrupt drops in QE curve at some particular wavelengths. However, not only the basic quantum efficiency measurement was employed but the lock-in amplifier technique was also used in this system in order to enhance signal-to-noise ratio. The results of both techniques were compared and exhibited an improvement of data acquisition. Finally, the effect of voltage bias applied to solar cells for demonstrating more realistic performance was observed. The results showed slight reduction of the photocurrent collection due to narrower space-charge region when solar cells operate in practical condition.

Department: Physics Student's Signature .....
Field of Study: Physics Advisor's Signature .....
Academic Year: 2014

ACKNOWLEDGEMENTS

First of all, I would like to express my deepest gratitude to my thesis advisor, Assistant Professor Dr. Sojiphong Chatraphorn who always give me valuable suggestions. He inspired many great ideas and gave me chances to improve my scientific skills. Without his guiding, this thesis cannot nicely succeed.

Besides my advisor, I would like to thank my thesis committee: Assistant Professor Dr. Rattachat Mongkolnavin, Assistant Professor Dr. Tonphong Kaewkongka and Dr. Rachsak Sakdanuphab, for their valuable opinions and comments on my work, especially some important points that have been disregarded.

I would like to thank Semiconductor Physics Research Laboratory (SPRL) members; Assistant Professor Dr. Kajornyod Yoodee for his advice, especially recommendations of useful books and theoretical knowledge sources in the early days of this work, Miss Busarin Noikaew and Miss Boonyaluk Namnuan for their photovoltaic devices used in this study as well as their practical teaching in thin film fabrications.

I would like to thank Mr. Pornsak Panchawirat from the Thailand Center of Excellence in Physics (ThEP Center) for theoretical knowledge and helping with energy dispersive x-ray spectroscopy (EDS) measurements.

I would like to acknowledge the financial supports from the ThEP Center, the Asahi Glass foundation, the Special Task Force for Activating Research (STAR), Ratchadaphiseksompot Endowment Fund, Chulalongkorn University through the Energy Materials Physics Research Group.

Finally, morale encouragement from my family for studying in master degree is a valuable thing I cannot forget to thank and appreciate.

CONTENTS

Page

LISTS OF TABLES

LISTS OF FIGURES

Page

LISTS OF SYMBOLS AND ABBREVIATIONS

η	Solar cell efficiency
ADC	Analog-to-digital converter
Al	Aluminum
AM1.5	Air-Mass 1.5
AM1.5G	Air-Mass 1.5 Global radiation
CBD	Chemical bath deposition
CdS	Cadmium sulfide
CGS	Copper-gallium-diselenide
CIGS	Copper-indium-gallium-diselenide
CIS	Copper-indium-diselenide
DUT	Device under test
E_{bi}	Built-in electric field
E_c	Conduction band edge
EDS	Energy dispersive X-ray spectroscopy
E_F	Fermi energy
E_{Fi}	intrinsic Fermi energy
E_g	Bandgap energy
EQE	External quantum efficiency
E_t	Trap state energy
E_v	Valence band edge
FF	Fill factor
Forw	Forward bias (voltage bias)
I_{in}	Input current (current-to-voltage circuit)
IQE	Internal quantum efficiency
I_{SC}	Short-circuit current
i-ZnO	Intrinsic zinc oxide
J-V	Current density-Voltage

J_D	Diode current density
J_{diff}	Diffuse current density
J_{drift}	Drift current density
J_L	Photogenerated current density
J_{MP}	Maximum power point current density
J_{SC}	Short-circuit current density
Mo	Molybdenum
PV	Photovoltaic
QE	Quantum efficiency
REF	Reference device
Rev	Reverse bias (voltage bias)
R_S	Series resistance
R_{SH}	Shunt resistance
SCR	Space-charge region
SDL	Surface defect layer
SEM	Scanning electron microscopy
Si	Silicon
SIMS	Secondary ion mass spectroscopy
SLG	Soda-lime glass
SMU	Source-measurement unit
SR	Spectral response
SRH	Shockley-Read-Hall
V_{MP}	Maximum power point voltage
V_{OC}	Open-circuit voltage
V_{out}	Output voltage (current-to-voltage circuit)
V_{output}	Output direct current voltage (lock-in)
V_{sum}	Summed voltage (lock-in)
x	[Ga]/([In]+[Ga])
ZnO(Al)	Aluminum doped zinc oxide

CHAPTER I

INTRODUCTION

1.1 Overview

Solar energy is well known as one of the cleanest and powerful renewable energy source for all lives on the Earth which consists of light and heat radiated from the Sun. Solar energy is, however, vast and abundant because one hour of irradiation provides more energy than the world needed for one year [1]. A tale of ancient Greek scientist, Archimedes who used the sunlight reflection from bronze shields to burn enemy ships in early 212 B.C. is an example for saying that human has been learning to use solar energy more than two thousand years ago [2]. By scientific and technological advances in the present, solar energy can not only be directly used as heat and light but it can also be shaped into other forms. Solar cells or photovoltaic (PV) devices are human inventions for converting photon energy into electric energy which is the most applicable form in daily life. Solar cell technology is being interested as a choice of alternative energy sources for solving energy crisis in the future as the energy demands continuously increase.

The origin of solar cells began from a discovery of photovoltaic effect, the most basic principle of solar cells, by Alexandre Edmond Becquerel in 1839 [3, 4]. A few decades later, Willoughby Smith discovered the photoconductivity in selenium solid material [5]. An attempt to prove that sunlight energy could be converted to electrical power without heat or moving part became an interesting even if selenium solar cells produced by William Grylls Adams and Richard Evans Day failed to demonstrate [6]. Until 1883, Charles Fritts was credited for creating the first genuine selenium solar cell [7]. His selenium wafer coated by a very thin layer of gold had conversion efficiency less than 1%. The photoconductivity was then found in various materials by many scientists in the same period as the discovery of the photoelectric effect. The modern age of solar cell technology began when Russell Shoemaker Ohl

Figure 1 Gerald Pearson, Daryl Chapin and Calvin Fuller (left-to-right) in Bell Labs who were credited for developing the first capable silicon solar cell [8].

who discovered a p-n junction in 1939 invented the first silicon solar cell by developing his work with diodes in 1941 [9, 10]. However, the early selenium and silicon solar cells were still inefficient for used in everyday equipment until the three scientists of Bell Telephone Laboratories, Gerald Pearson, Calvin Fuller and Daryl Chapin, successfully invented a capable silicon solar cell with 6% conversion efficiency in 1954 [11]. Although this success led to rapidly enhanced silicon solar cell efficiency in short term, they were still being applied in few devices because of their extremely high cost. Major use of solar cell were in field of space applications after arrays of silicon solar cell were firstly brought to the space with the Vanguard I, the U.S. satellite, as a power source in late 1950s. Solar cell technologies were then continuously developed as the world technologies go forward.

In the present day, many researchers throughout the world are concentrating to develop their solar cell technologies. Many new materials were discovered as well as new construction designs were improved. And because of its lower price than the past and its worthiness in long term, this technology attracts many peoples who are looking for alternative ways to economize energy consumption cost.

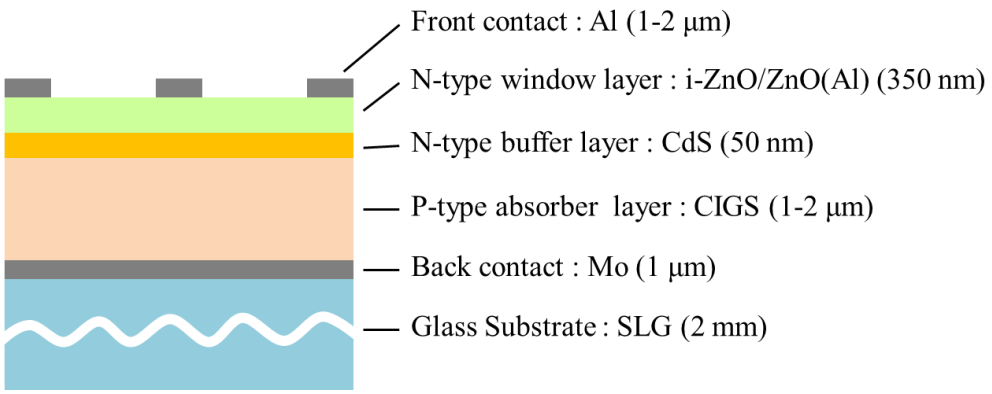

Figure 2 A typical structure of standard CIGS heterojunction thin film solar cell.

Among many solar cell materials, Copper-indium-gallium-diselenide ($CuIn_{1-x}Ga_xSe_2$ or CIGS) ternary compound semiconductor is one of the promising materials for creating high efficiency solar cells. The strengths of CIGS are not only its high absorption coefficient and suitable bandgap energy (E_g) but also the sun light spectra matching. The CIGS thin film solar cells have been continuously developed for more than decades and the latest world record efficiency of this solar cell is at 21.7% produced by ZSW [12]. Figure 2 shows a standard structure of CIGS solar cells that can be achieved by common thin film fabrication techniques.

For device characterizations, there are many methods used to study the properties and demonstrate the solar cell performances. Especially the charge carrier or the photogenerated current collection of a solar cell, quantum efficiency (QE) measurement becomes a good choice. The quantum efficiency is used to indicate the ability to generate photocurrent when a solar cell is illuminated by photons of a particular wavelength. Although the photogenerated current collected from a solar cell can be measured by a current density-voltage (J-V) measurement which is revealing in term of the short-circuit current density (J_{SC}), the results do not give much detailed information. In other words, in J-V measurement, polychromatic light is applied on a cell. This means the currents are generated from photons of all wavelengths and from all thin layers comprising a device. Conversely, monochromatic light is applied on a cell in QE measurement. So the photocurrents are generated from each layer of

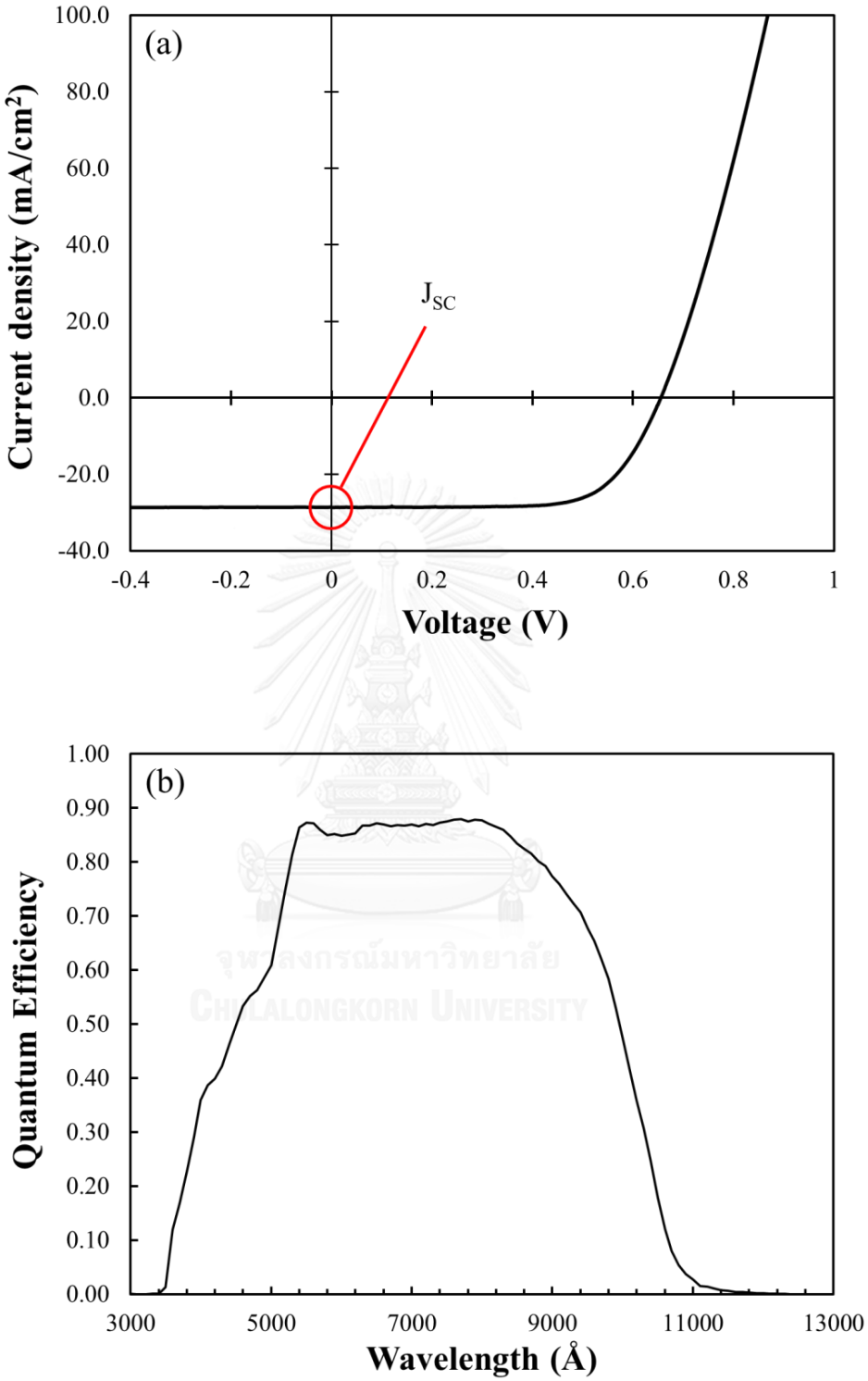

Figure 3 The information of photogenerated currents are revealed as (a) the short-circuit current density J_{SC} in J-V characteristic curve, and (b) QE curve.

material that has bandgap energy corresponds to the incident photons. Figure 3 shows the J-V and QE curves where details of the current collection are more revealed in QE measurement. It would be better if some details e.g. the carrier generation, the carrier collection and the defects in each thin layer can be studied. Therefore, by using QE measurement together with other characterizations, not only the overall current conversion efficiency is determined, but also the properties of each thin film layer can be investigated.

For the main parts of this study, a quantum efficiency measurement system was constructed and performed to study the effect of various fabrication conditions of the CIGS thin films on the photogenerated current collection. The defective devices with poor performance were also investigated to identify the causes of problems. In addition, not only the basic QE measurement was used but the lock-in technique was also applied to this system in order to enhance the measuring signals. Moreover, to demonstrate solar cell performance as in practical operating condition, voltage bias was applied to solar cells during QE characterization.

1.2 Objectives

1) To construct a QE measurement system for photovoltaic devices.

2) To study the effect of different deposition conditions of the CIGS absorber layer on the photogenerated current collection by the QE measurements.

3) To use the QE measurements to identify the cause of current loss.

4) To improve the signal-to-noise ratio in the QE measurement by adding the lock-in technique.

5) To study the photoresponse of solar cells in realistic operating condition by applying voltage bias.

1.3 Thesis outline

This thesis is divided into five chapters. In chapter II, some theoretical backgrounds, for example, material properties of CIGS, the photovoltaic effect, the quantum efficiency and characterization techniques are introduced. The concepts of system setup design as well as the controlling programs are then discussed in chapter III. After that, the experimental details together with their results which can be divided into four subtopics are discussed in chapter IV. Finally, the last chapter is the summary of this study.

CHAPTER II

THEORETICAL BACKGROUNDS

2.1 $CuIn_{1-x}Ga_xSe_2$

2.1.1 Material properties

$CuIn_{1-x}Ga_xSe_2$ or $Cu(In,Ga)Se_2$,or in short CIGS, is an alloyed semiconductor in the family of I-III-VI_2 that is formed from two ternary compounds: $CuGaSe_2$ (CGS) and $CuInSe_2$ (CIS). The crystal structure of these compounds is tetragonal chalcopyrite which can be imaged by stacking two cubic zinc blends of II-VI materials, like ZnSe, as shown in figure 4, where Cu (group I) atom and In (or Ga) (group III) atoms occupies in the site of Zn such that each Cu and In/Ga is surrounded by four Se atoms. Although this chalcopyrite is formed by two cubic unit cells, the lattice constant c is not exactly two due to differences in bond strengths of I-VI and III-VI bonds [13].

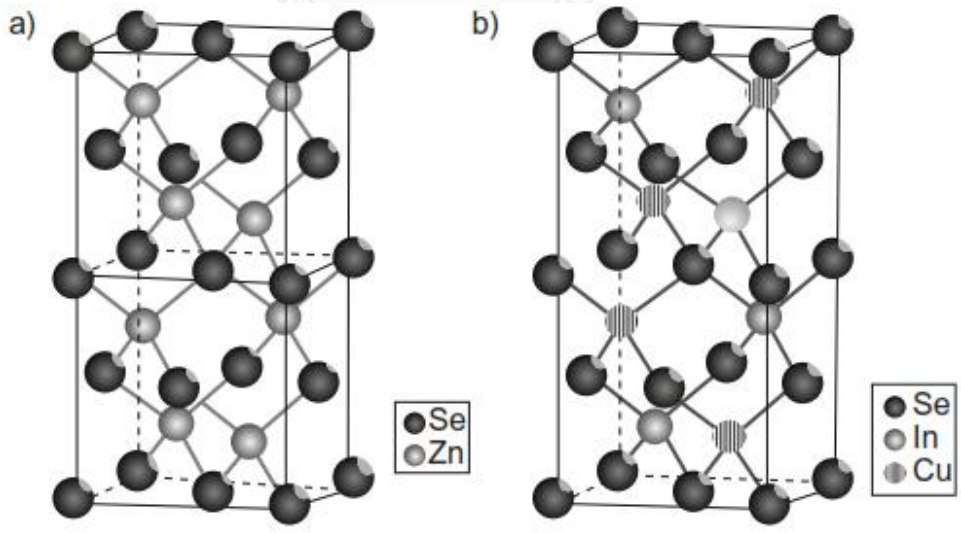

Figure 4 Crystal structures of chalcogenide compounds. By replacing Cu and In in the atomic site of Se in (a) double cubic zinc blend structure of ZnSe, (b) tetragonal chalcopyrite structure of $CuInSe_2$ can be obtained [13].

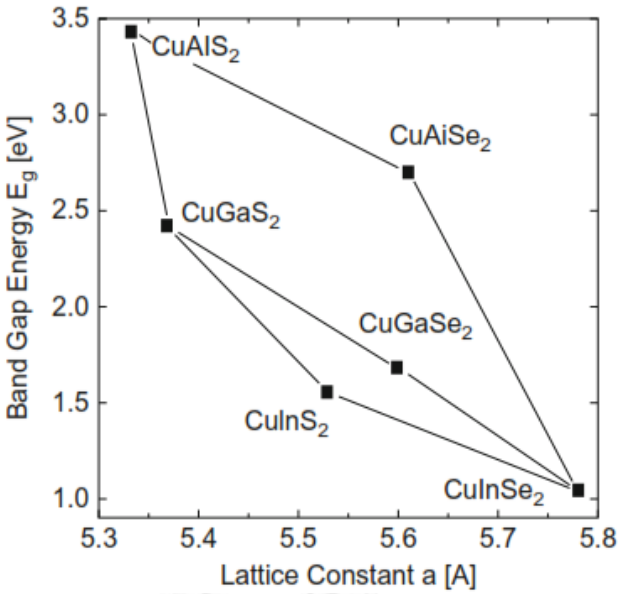

Figure 5 Bandgap energy as a function of lattice constant a of the entire $Cu(In,Ga,Al)(Se,S)_2$ alloy system [13].

Since $CuIn_{1-x}Ga_xSe_2$ is an alloyed material, its bandgap energy E_g given by eq. 1 can be adjusted between 1.04 eV ($E_{g,CIS}$) and 1.68 eV ($E_{g,CGS}$) depending on the elemental composition ratio, $x=[Ga]/([In]+[Ga])$, [14]

$$E_{g,CIGS}(x)=(1-x)E_{g,CIS}+xE_{g,CGS}-bx(1-x), \quad (1)$$

where b is the bowing parameter (0.15-0.24 eV). In addition, the entire $Cu(In,Ga,Al)(Se,S)_2$ chalcopyrite system can provide bandgap energy up to 3.4 eV in $CuAlS_2$ as shown in the relationship between lattice constant a and bandgap energy in figure 5.

There are reasons for CIGS to be an interesting and promising material in solar cell community. Firstly, CIGS has a direct bandgap which the photon absorption can easily take place at the same wave vector. No phonon energy, the energy of a lattice vibration, is needed for the transition of valence electrons to the conduction band like in case of indirect bandgap material (for example, Si). Therefore, direct bandgap materials are suitable for photovoltaic devices. Second, the absorption coefficient of

CIS (and also CIGS) is highest compared to other solar cell materials as shown in figure 6. At last, figure 7 shows the theoretical calculation of the conversion efficiency %η as a function of bandgap energy E_g of various solar cell materials. It indicates that CIGS alloy has potential to be high efficiency devices which the maximum efficiency can go up to about 30%.

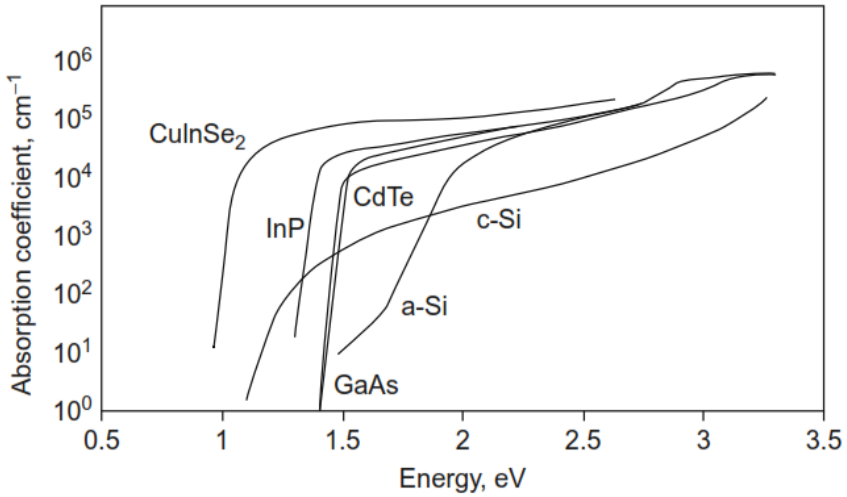

Figure 6 Absorption coefficients versus photon energy of various semiconductors [15].

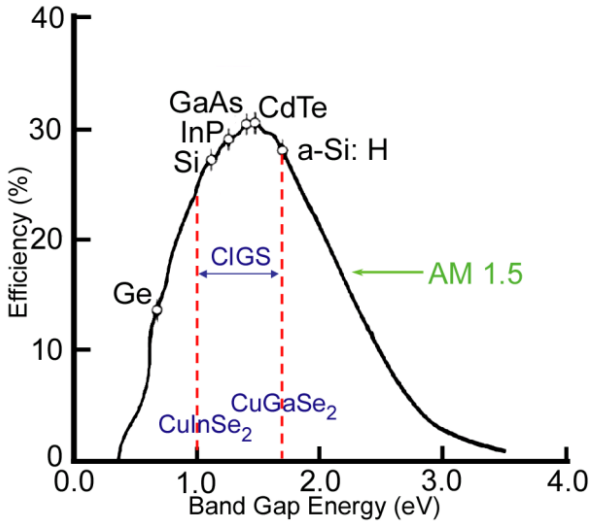

Figure 7 Theoretical efficiencies of several solar cell materials. This is also known as "Shockley-Quisser approximation" which demonstrates the efficiency limitation for one-junction devices [16].

2.1.2 $CuIn_{1-x}Ga_xSe_2$-based thin film solar cells

The history of CIGS solar cells began with only CIS which Hahn et al. could synthesize in 1953 [17]. A mono-crystalline CIS solar cell was then exhibited 12% conversion efficiency in 1974 [18]. In 1983-1984, efficiency excess of 10% for thin film poly-crystalline was fabricated by three-source co-evaporation process by Boeing Corp [19]. Until 1990, Devaney et al. reported a noticeable improvement after partially replacing In with Ga in the absorber layer [20]. Some works suggest that the enhancement of band gap matching to solar spectrum and the improvement of electronic properties could be observed when the cells were fabricated with 20-30% of Ga [21, 22].

The fabrication of standard CIGS heterojunction thin film solar cells as shown in figure 2 (section 1.1) can be briefly described as follows. Mo with 1 μm thick serves as a back contact which is sputtered upon 2 μm thick soda-lime glass (SLG) substrate. The CIGS absorber layer with thickness of 1-2 μm is then deposited by multi-sources co-evaporation. The p-n heterojunction is formed after coating of 50 nm thick of CdS buffer layer by means of chemical bath deposition (CBD). Transparent window layers of 350 nm thick consists of intrinsic ZnO (i-ZnO) and heavy Al dope of ZnO (ZnO(Al)) is sequentially sputtered on top of CdS to complete the heterojunction. Finally, Al of 1-2 μm thick is deposited as front contact grid to finish a solar cell. Anyway, one can get more detailed information about the CIGS solar cell fabrication from [23-25].

Figure 8 shows the one-dimensional band diagram of the ZnO/CdS/CIGS heterojunction which the discontinuities of conduction band edge E_c and valence band edge E_v appears because of differences in bandgap energies and types of doping. At the CdS/CIGS interface, there is a 10-30 nm thick of surface defect layer (SDL). The physical natures of this defect layer are under debate and still not clearly understood in playing an important role affecting the overall performance of the devices.

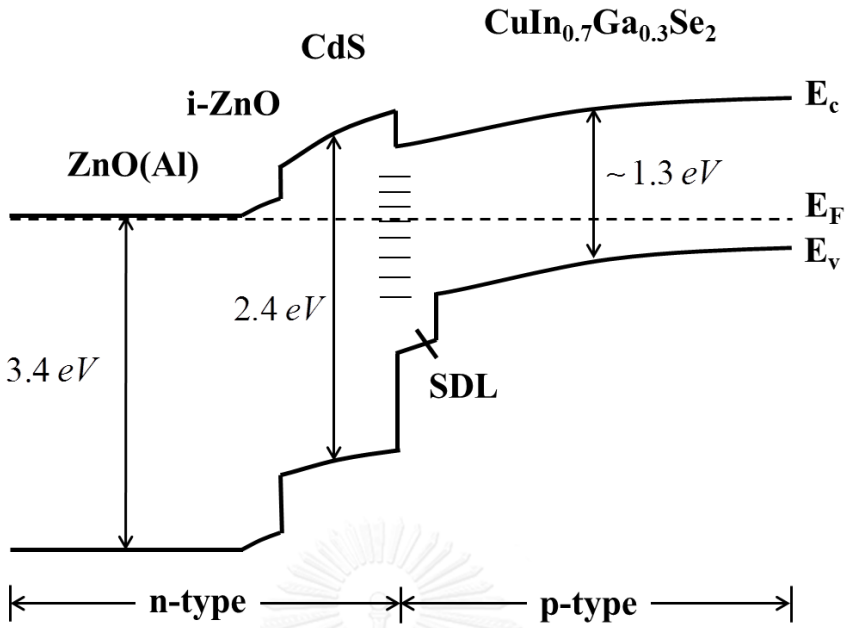

Figure 8 One-dimensional energy band diagram of the ZnO/CdS/CIGS heterojunction showing p-n junction and surface defect layer (SDL) together with interface recombination centers at the CdS/CIGS interface.

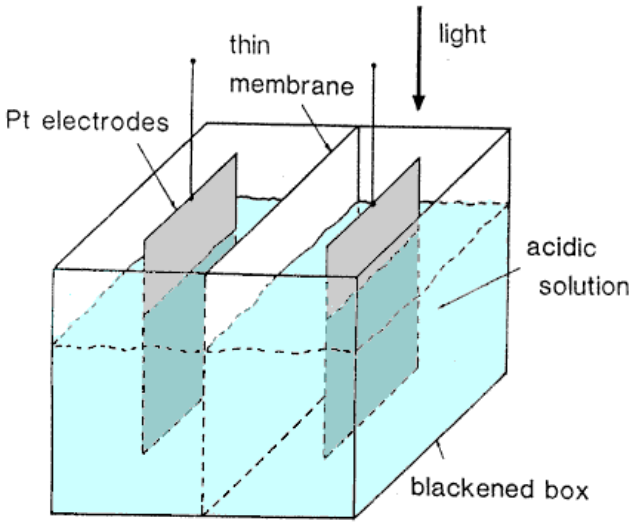

Figure 9 Setup diagram in Becquerel's experiment [26].

2.2 Photovoltaic effect

The photovoltaic effect was firstly discovered by A. E. Becquerel in 1839 while experimenting with platinum electrodes placed in an acidic solution as depicted in figure 9. Under illumination by various types of light sources including sunlight, he observed the generation of voltage and current. Because of this work, the discovery was known as “Becquerel effect”.

From the origin of the name that made up from *photo* (came from Greek word, *phos = light*) and *voltaic* (came from the name of Italian physicist, Alessandro Volta, *voltaic = related to electricity*), the photovoltaic effect is the effect involves electricity produced from light. Although Becquerel’s work dealt with liquid solution while most of nowadays solar cells are solid materials, the principle is still the same. The photovoltaic effect is a fundamental principle governing the operation in solar cells and consists of main processes as described in follows.

2.2.1 The charge carrier generation and recombination

In thermal equilibrium in any intrinsic and extrinsic (or doped) semiconductors, the charge carriers: electrons and their leaving unoccupied states in the valence band which have positive charge, so-called holes, can be generated randomly by thermal process. However, a pair of an electron and a hole can also be annihilated by recombination which is a reverse process of pair generation. The rates of generation G and the rate of recombination R must be equal in order to balance the numbers of carriers in equilibrium and are given by [27]

$$G_{n0} = G_{p0} = R_{n0} = R_{p0} \tag{2}$$

where the subscribed $n0$ and $p0$ denote electrons and holes in equilibrium condition, respectively. Units of G and R are $[\#/cm^3 \cdot \sec]$.

However, if there is an external excitation such as light, the excess electrons and holes can also be generated by the photon absorption and resulting in non-equilibrium condition. Figure 10 schematically exhibits the electron-hole pair generation and recombination processes involved with optical absorption.

The rates of electron-hole pair generated within the device are not constant. If we assume that the loss of light intensity directly causes the photon absorption, and since the decreasing of light intensity into the bulk is an exponential decay, thus electron-hole pair generation function can be written as [28]

$$g'_n = g'_p = g'_0 \exp[-\alpha(\lambda) \cdot x] \tag{3}$$

where g'_0 is the generation rate at the front surface, $\alpha(\lambda)$ is the absorption coefficient, x is the depth from the front surface through material thickness. The generation rate G' per unit volume can be expressed by $G' = g'/A$, where A is the photon illumination area on the device. For different photon wavelengths, the shorter is more likely to be absorbed near the front surface than the longer photon wavelength because of its higher energy as shown in figure 11.

For the recombination in non-equilibrium, the recombination rates for electrons and holes under the low injection condition, the excess carriers concentration is much lower than the concentration of majority carriers, are given by [27]

$$R'_n = R'_p = \frac{\delta n(t)}{\tau_0} \tag{4}$$

where $\delta n(t) = \delta p(t)$ is the concentration of the excess carriers, τ_0 is the average minority carrier lifetime (τ_{n0} for p-type material and τ_{p0} for n-type material). The average lifetime refers to the mean time until carriers are recombined.

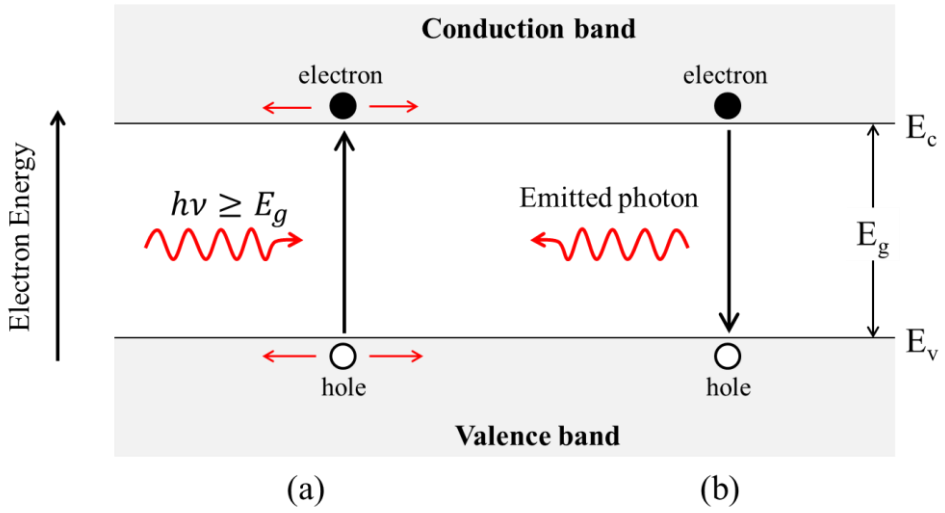

Figure 10 (a) The band-to-band generation via photon absorption and (b) the band-to-band recombination in semiconductors.

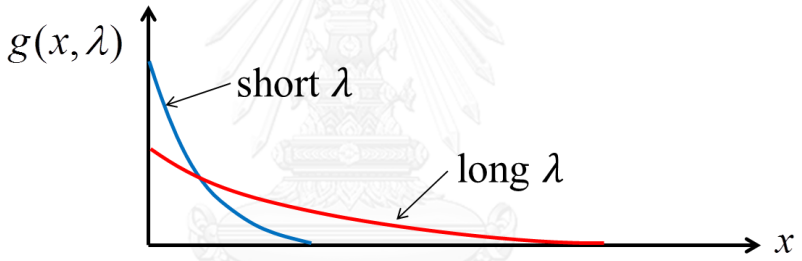

Figure 11 The generation functions for different photon wavelengths.

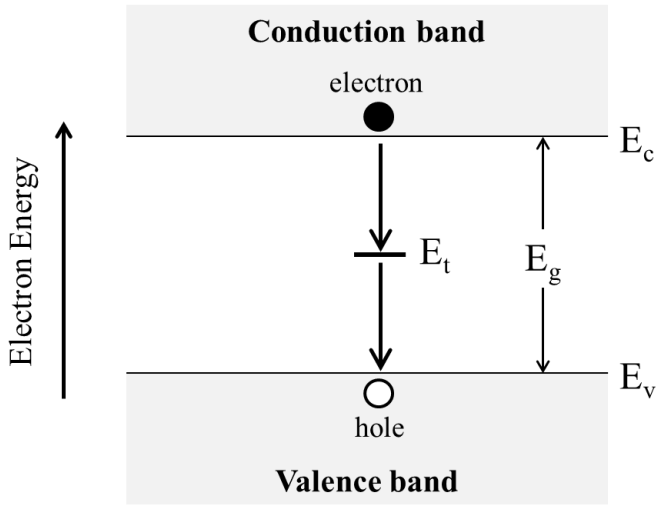

Figure 12 The Shockley-Read-Hall recombination.

In real semiconductors, the carriers can be recombined not only by the band-to-band process but also via defects from imperfection of the crystals. If the concentration of defects is not so high, the discrete defect states or traps will be created in the bandgap as shown in figure 12. A trap where electrons or holes can be captured is called a recombination center. This recombination mechanism is called the Shockley-Read-Hall (or SRH) recombination which named after William Shockley, William Read and Robert Hall who introduced in 1952 [29, 30]. However, surfaces and interfaces also have defects e.g. grain boundaries, broken bonds and impurities. Since these defects are in higher concentration than in case of bulk, therefore the recombination rate at surfaces or interfaces is higher and the excess carrier lifetime is also shorter. The surface recombination velocity $[cm/\sec]$ is usually used to characterize the surface properties of materials which indicate how fast carriers move to surface to recombine.

The trap-assisted recombination, especially at the interfaces, significantly impacts on the properties of semiconductor devices. In practice, a passivative layer is coated (for example, oxide layer on silicon surface) to reduce the recombination rate by preventing carriers to reach the surface. In case of the CdS/CIGS interface, a high barrier shown as the band offset, 'the spike', between conduction band edges of CdS and CIGS in figure 8 is preferred to minimize the interface recombination [31].

2.2.2 The charge carrier collection

The concept of carrier collection can be understood by using an ideal p-n diode model. A short moment after connecting p-type and n-type semiconductors together, the unequal in their concentrations would drive majority carriers in each side (electrons in n-side and holes in p-side) to diffuse across the interface into another side and form the p-n junction. This phenomenon, on the other hand, is described as a result of the potential energy gradient in band diagram of p-n junction figure 13. The region that built-in electric field $\vec{E}_{bi}$ generated and deplete of charge carriers is called the space-charge region (SCR). In the case of CIGS herojunction, the SCR occupies deep into the CIGS absorber bulk due to highly n-type doping of ZnO and CdS layers.

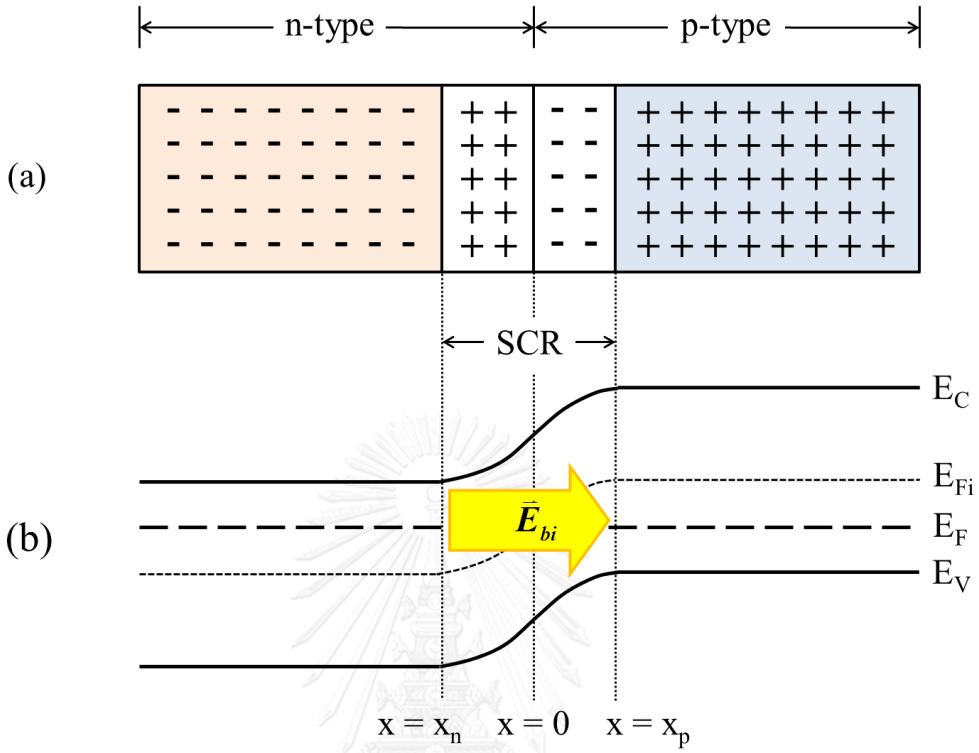

Figure 13 The p-n junction is formed by contacting n-type and p-type semiconductors. (a) The majority carriers in each region. (b) The band diagram of p-n junction where the built-in electric field $\vec{E}_{bi}$ is created from band bending.

Let's consider the thermal equilibrium. When an external circuit such as a load, is connected to both electrodes of the p-n diode, the charge carriers are randomly generated and recombined within the diode. One can expect the current density flow out to external load or so-called the collected current density to be zero due to equal in the rates of generation and recombination.

When the diode is stimulated by photon illumination, it is no longer in equilibrium. The generated excess carrier electrons and holes are then separately drifted by influence of built-in electric field. If one assumes that all carriers generated in the SCR can be separated, these carriers will contribute to be the collected current. On the other hand, the minority carriers those generated outside the SCR must diffuse

to the junction in order to be collected by external circuit. Unfortunately, they are likely to be recombined with abundant majority carriers if they have short diffusion lengths. The ideal total photogenerated current density which is a summation of these drift and diffusion current densities as shown schematically in figure 14 is expressed by [27, 28]

$$J_L = e\left(W + L_n + L_p\right)G' \tag{5}$$

where e is the electronic charge, W is the SCR width, L_n and L_p are the average diffusion length of minority carrier electrons and holes, respectively. The diffusion length is the distance that carriers can move before being recombined. The generation rate of excess carriers G' is assumed to be uniform entire the device. In addition, this total collected current density is sometimes called a short-circuit current density J_{SC} because no external bias voltage is applied and the diode is short circuited. However, it is difficult to derive the photogenerated current in real solar cells due to many complex parameters e.g. non-uniform generation rate, non-uniform impurity doping, recombination with trap states inside the bulk and interfaces, etc.

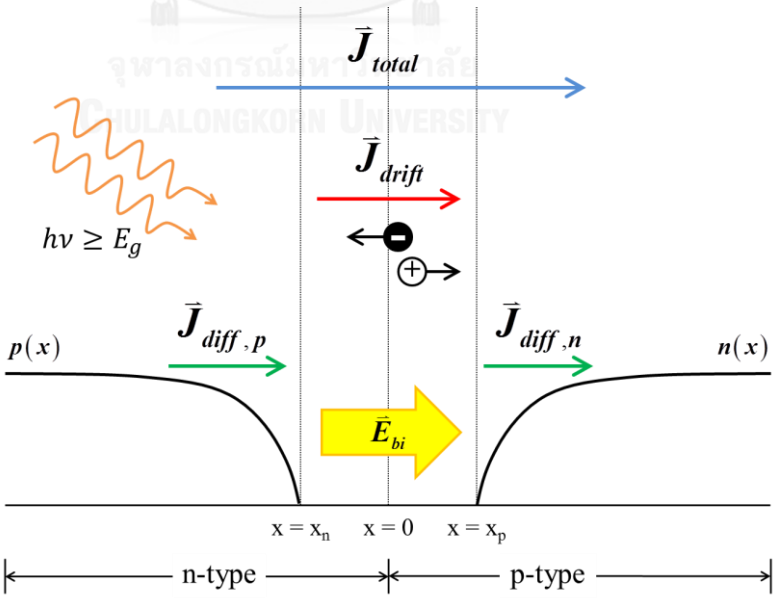

Figure 14 The ideal total photogenerated current comprises of the drift current within the SCR and the diffusion currents due to non-uniform charge carrier concentrations in the bulk.

2.3 Solar cell characterizations

2.3.1 J-V characteristics

The current density-voltage (J-V) measurement, or more often current-voltage (I-V), is a most common and very important measurement for photovoltaic devices. This technique is used to demonstrate the device performances via the photovoltaic parameters: the short-circuit current density J_{SC}, the open-circuit voltage V_{OC}, the fill factor FF, which are deduced from J-V characteristic curve as shown in figure 15b.

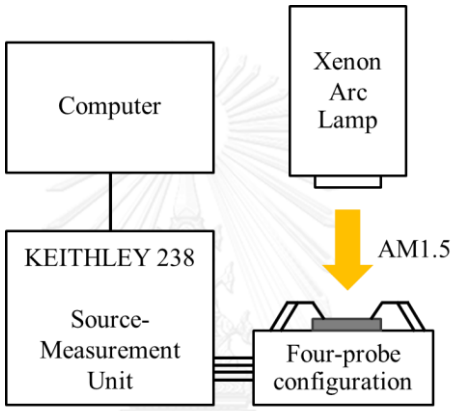

(a) The J-V measurement setup

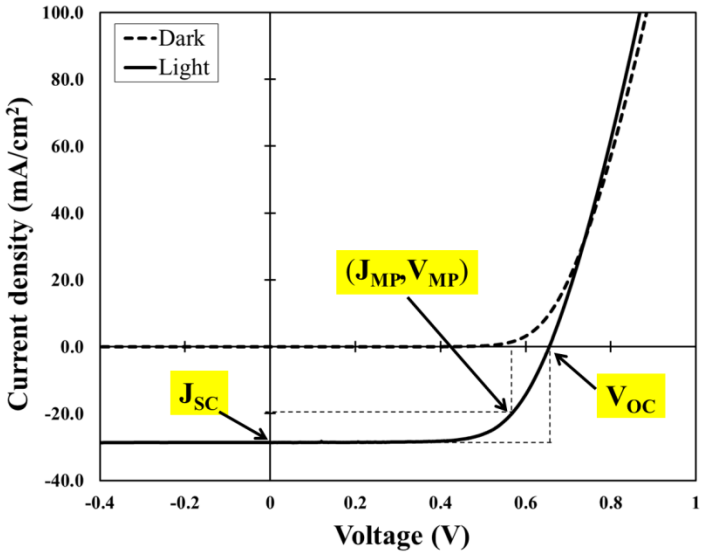

(b) J-V characteristic curves

Figure 15 A typical schematic diagrams for J-V measurement and J-V characteristic curves showing three important photovoltaic parameters.

To obtain the curves, a varying voltage V is biased to the front and back electrodes and the current I ($I = J \cdot A$, where A is the cell area) is then measured or vice versa. Under photon illumination with, for example, Air-Mass 1.5 (AM1.5) standard condition (approximately 100 mW/cm^2), the light J-V curve obeys the Shockley diode equation which in the simplest form as

$$J = J_0 \left[\exp\left(\frac{eV}{nk_B T} \right) - 1 \right] - J_L \tag{6}$$

where J_0 is the reverse saturation current density serving as a reminder that a solar cell in the dark is simply a diode, n is the diode ideality factor. The values of J_0 and n depend on the dominant recombination process within the device [32, 33]. The photogenerated current density J_L is usually equal to the short-circuit current density J_{SC} in the short-circuit operating condition (or $V = 0$). Although the superposition principle held in eq. 6 implies that the lighted curve is shifted from the dark term by a constant J_L, the photocurrent can be voltage dependent and the light curve might show different properties from the dark in real solar cells. Therefore, a crossing between the curves of illuminated J-V and the dark J-V, which is called the cross over effect, can be observed [34, 35].

The open-circuit voltage V_{OC} is the voltage difference between two electrodes when a cell is illuminated but not connected to an external load. It is also related to the bandgap energy and recombination of the absorber. By taking no collected current flow $J = 0$ condition into eq. 6, the V_{OC} is given by

$$V_{OC} = \frac{k_B T}{q} \ln\left(1 + \frac{J_L}{J_0} \right). \tag{7}$$

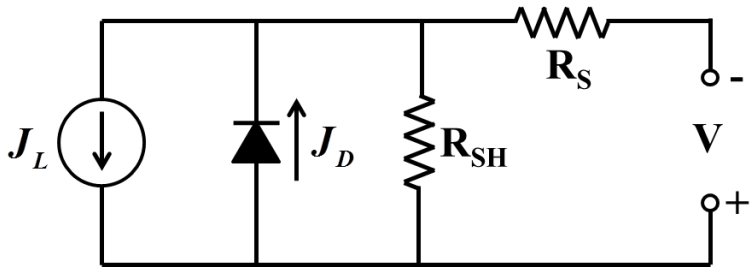

Figure 16 An equivalent circuit of a practical solar cell. A p-n heterojunction is depicted as a diode of diode current density J_D, a current source denotes the photogenerated current density J_L, R_S and R_{SH} are the series and shunt resistances, respectively. Since J_L has opposite direction to the forward diode current density J_D, the J-V curves gives negative J_{SC}.

Since practical solar cells usually have the parasitic resistance as shown in the equivalent circuit figure 16, the extended Shockley equation becomes

$$J = J_0\left[\exp\left(\frac{q(V - JR_S)}{nk_BT}\right)\right] + \frac{V - JR_S}{R_{SH}} - J_L \tag{8}$$

where R_S is the series resistance accounting for the resistance of current paths in layers and contacts, while the shunt or parallel resistance R_{SH} usually refers to resistance of small parallel paths through or around the device layers, and also implies the current leakage that is affected by defects at the p-n junction. In an ideal case, very small series ($R_S \to 0$) and infinitely large shunt ($R_{SH} \to \infty$) resistances are preferred.

The fill factor FF is defined as the ratio of the maximum output power density to the product of J_{SC} and V_{OC},

$$FF = \frac{J_{MP}V_{MP}}{J_{SC}V_{OC}} \tag{9}$$

It measures the squareness of a J-V curve. Typically, FF is between 0.7 and 0.85 for high efficient solar cells.

The conversion efficiency of a solar cell is defined as a ratio of the maximum output electrical power to incident optical power, one can write

$$\eta = \frac{P_{out}}{P_{in}} = \frac{J_{MP}V_{MP}}{P_{in}} = \frac{J_{SC}V_{OC}FF}{P_{in}} \tag{10}$$

where the incident power $P_{in} = P_{AM1.5} = 100$ mW/cm^2 if AM1.5 is used.

2.3.2 Quantum efficiency and Spectral response

The quantum efficiency QE indicates the amount of photogenerated current produced when a solar cell is illuminated by photons of a particular wavelength. It is defined as

$$\mathrm{QE}(\lambda) \equiv \frac{\text{number of collected electrons}}{\text{number of incident photons}} = \frac{I_{SC}(\lambda)/q}{\Phi_{ph}(\lambda)}. \tag{11}$$

where $I_{SC}(\lambda)$ is the photogenerated current in unit of $[A]$, and $\Phi_{ph}(\lambda)$ is the incident photon flux in unit of $[\#/\sec]$. In other words, the QE is a probability that an incident photon of wavelength λ will be absorbed and then deliver an electron to an external circuit.

Since the QE is described as a probability, the ideal QE is equal to one. Whiles the actual QE is reduced from unity by many factors as described in the below list and shown in figure 17 for the case of CIGS devices:

(i) *Grid shading*. The front contact grid is usually used in standard CIGS devices. If incident photons are shined cover whole cell area, there would be losses in overall photogenerated current and also QE spectrum.

(ii) *Reflection*. Some portion of incident photons is reflected from the front surface of each thin layer due to the effect of refractive indices. This loss can be reduced by coating an anti-reflection layer, for example, MgF_2.

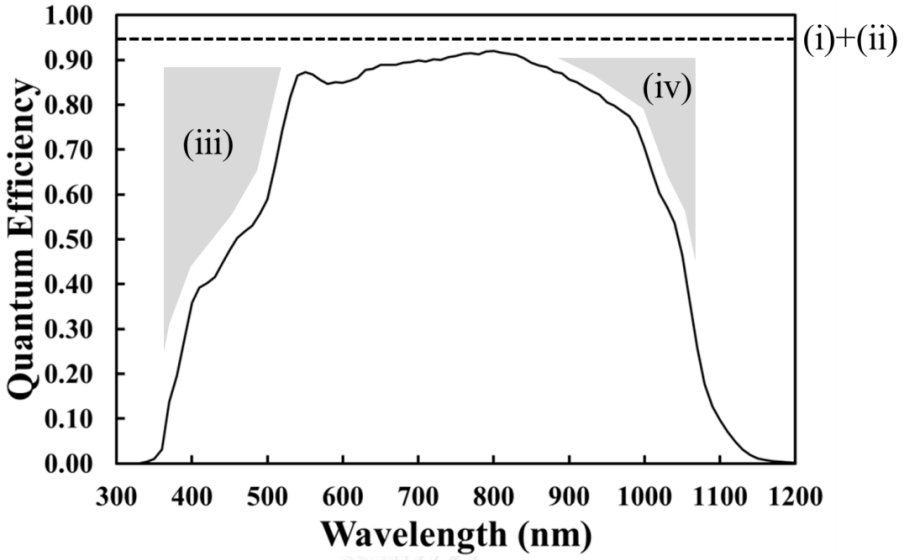

Figure 17 An QE spectrum of a CIGS solar cell showing the factors causing the current losses as labeled in each region.

(iii) *Window and buffer absorptions*. Charge carriers generated by optical absorption in ZnO window and CdS buffer layers are affected by heavy n-type doping. They would have a short lifetime and cannot diffuse to the SCR. Thus, large number of carriers is recombined and cannot distribute to collect photocurrent.

(iv) *Incomplete collection*. Some of charge carriers deep in CIGS absorber bulk that generated by photon absorptions, especially long wavelength photons, are likely to be recombined before reaching the SCR. Moreover, high concentration of defects at the CdS/CIGS interface is also a factor resulting in incomplete current collection.

QE measurement, in general, is the measure of photocurrent in the short-circuit condition or I_{SC} for each incident photon wavelength. Besides the photoresponse revealed in a QE curve, the absorption edge at long wavelength shows the beginning of photon absorption, while the integrated area under a curve implies the total photogenerated current produced by a cell which can be calculated by

$$I_{SC} = q\int_{\lambda} \Phi_{ph}(\lambda)\cdot \mathrm{EQE}(\lambda)\, d\lambda \tag{12}$$

where $\Phi_{ph}(\lambda)$ is the incident photon flux of wavelength λ, and the integration is carried out overall wavelength λ of optical absorption.

Because the number of photocurrent collections is affected by all the thin film layers of the device, therefore, both overall current conversion efficiency and properties of each thin film layer can be investigated by the QE measurement. The details of instrumental setups as well as measuring techniques will be further discussed in chapter III.

However, QE can be divided into two types, the external QE (EQE) and the internal QE (IQE). The first is determined by including all incident photon with optical losses such as reflection and transmission. Conversely, the latter considers only photons that can generate charge carriers, not reflected or transmitted out of the cell. In this work, only EQE was reported while IQE can be obtained from $\mathrm{IQE} = \mathrm{EQE}/[1\text{-}R(\lambda)]$, where $R(\lambda)$ is the reflectance of the device.

Similar to quantum efficiency, the spectral response $\mathrm{SR}(\lambda)$ gives rather the same physical meaning but in different unit, $[A/W]$. It refers to the ratio of photocurrent generated by a cell to the spectral irradiance at each wavelength. Since irradiance relates to the number of photons, the spectral response can be written in term of quantum efficiency as

$$\mathrm{SR}(\lambda) = \frac{I_{SC}(\lambda)}{P(\lambda)} = \frac{q\lambda}{hc}\mathrm{QE}(\lambda) \tag{13}$$

where $P(\lambda) = \Phi_{ph}(\lambda)\cdot hc/\lambda$ is the spectral power density and h is the Planck's constant. Types of spectral response is decided by types of quantum efficiency is used.

2.3.3 Energy dispersive X-ray spectroscopy (EDS)

The EDS technique differs from previous two characterizations, it is used for analyzing the information of the elemental constituents in the specimen. The EDS can be performed as an optional analysis in the scanning electron microscopy (SEM).

After a high energy beam electron interacts with an inner shell (for example, K-shell, where the principle quantum number n = 1) electron of a specimen atom, an ejection of the shell electron is then take place. Since the atom is in excited state with a missing inner shell electron, it relaxes to ground state by the transition of an electron in the outer shell (for example, L-shell, n=2) to the inner shell vacancy. Because the outer shell state has more energy than the inner state, the excess energy has to be emitted as a photon as shown in figure 18. The wavelengths of photons emitted from the relaxation are in order of x-ray and are specific for each element. So these photons are called characteristic x-rays and are used to identify elemental proportion within the sample.

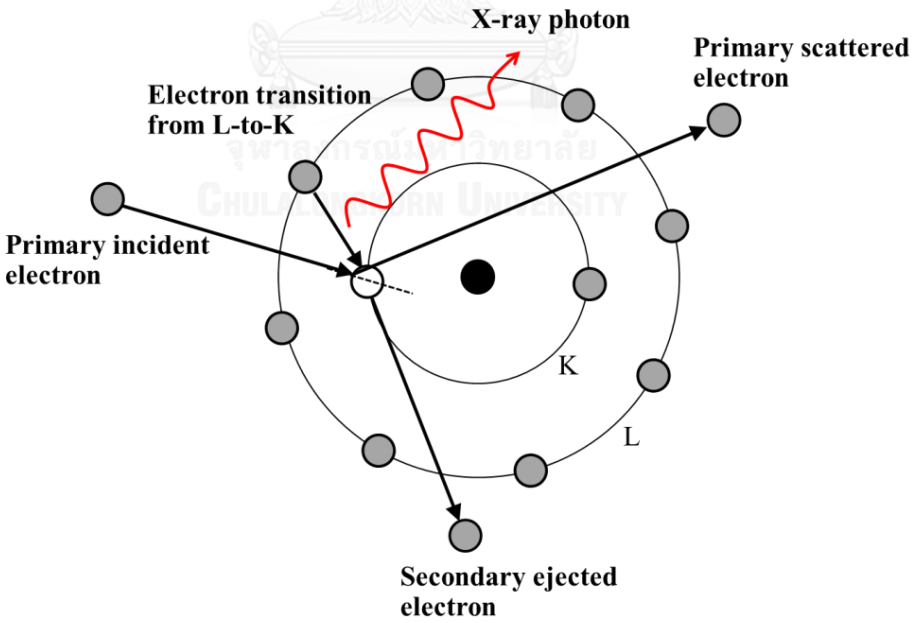

Figure 18 The characteristic x-ray emission by the electron transition from the L-shell to the vacant state in K-shell in a Ne atom.

The electron transition is more complicated when the atom has atomic number $Z \geq 11$. Not only L-to-K transition can occur but transitions in next further shells can also take place. Figure 19 shows schematic diagram of electron transitions and corresponding emitted x-rays. The name of x-ray line, for example, Kα, indicates the transition of electron from the next shell (L-shell) to the K-shell. Similarly, the Lβ x-ray is emerged from the occupying of an electron state in the L-shell by the next two shell (N-shell, n=4) electron. Moreover, each shell beyond the K-shell can be divided into subshells depends on the angular quantum number ℓ (ℓ = 0, 1, 2, …, n-1). The full detail of electron transitions between subshells can be found in [36].

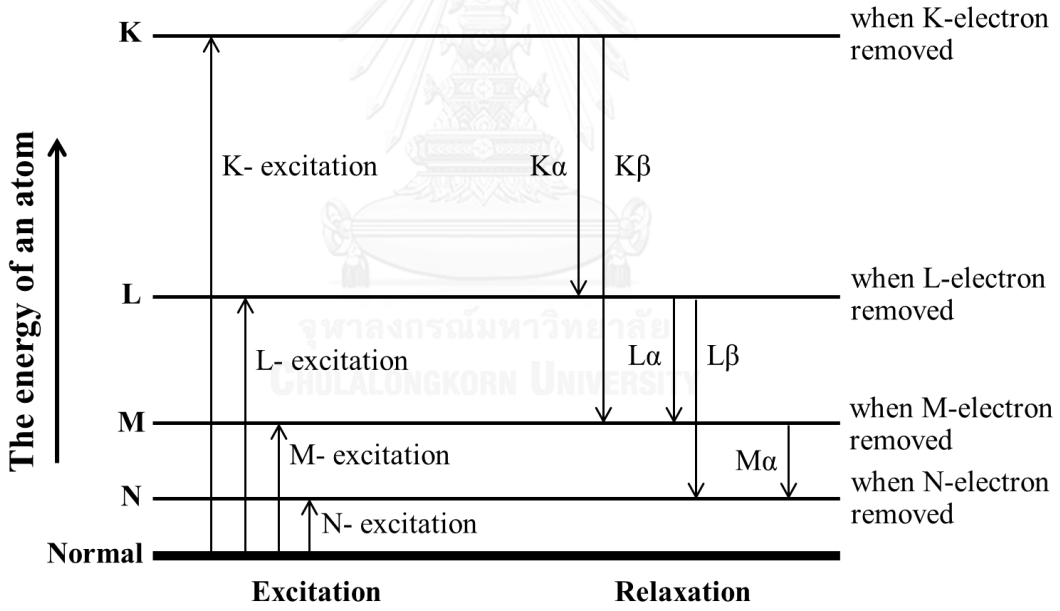

Figure 19 Energy diagram for electron transition. The energy of the atom will increase after excitation. Transition and x-ray emission are then occurred to reduce the energy.

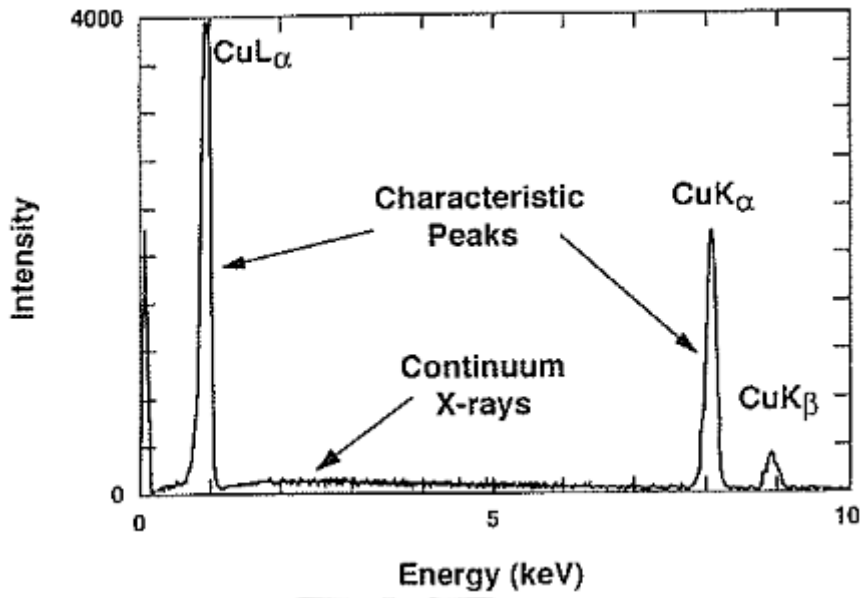

Figure 20 An example of EDS spectrum of copper showing x-ray characteristic peaks: CuLα, CuKα and CuKβ; and the bremsstrahlung continuum x-rays [32].

The EDS result is obtained by converting the out coming x-ray photons into voltage pulses in the detector and amplifier components. The characteristic x-ray peaks will be appeared and are then used to specify the elements together with corresponding proportions within the investigating area. Figure 20 is an example of EDS spectrum of copper, where the continuum backgrounds so called the bremsstrahlung or the braking radiation are caused from the Coulomb interactions between the incident electrons and the specimen atoms.

In this study, the EDS technique was performed to analyze the elemental composition in the absorber layers at different depth from front surface. These results were then used to calculate the composition depth profiles for each sample.

CHAPTER III

THE QE MEASUREMENT SYSTEM

3.1 Concept of QE measurement

To perform a QE measurement, one has to know the number of output electrons and the number of input photons. But it is difficult to be examined because those two numbers are not simply measured in practice. Therefore, they are measured in terms of the output current and the incident photon flux as expressed in eq. 11 (section 2.3.2).

However, a desired parameter, the incident photon flux $\Phi_{ph}(\lambda)$, is still complicated and difficult to measure in most QE systems. To overcome this trouble, measuring the relative QE is the easiest way. Thus, a QE result can be obtained by comparing short-circuit currents I_{SC} of the device under test (DUT) and the reference (REF) as in the following expression

$$\mathrm{QE}_{DUT}(\lambda) = \left(\frac{I_{SC,DUT}(\lambda)/\mathrm{A}_{DUT}}{I_{SC,REF}(\lambda)/\mathrm{A}_{REF}} \right) \cdot \mathrm{QE}_{REF}(\lambda) \qquad (14)$$

where the incident photon spot area A is taken into the calculation for getting the short-circuit current densities $J_{SC} = I_{SC}/\mathrm{A}$ such that the dependence of the current on photon spot size is eliminated. One has to remind that this calculation is valid if and only if the photon flux illuminated on both devices is equal. So the term in bracket acts as a factor for converting a QE spectrum of a reference for another unknown device. So in this measurement, QE reference data as a function of photon wavelength are needed as well as short-circuit current I_{SC} has to be measured.

3.2 The QE system setup

3.2.1 Light sources and optical path alignment

Since solar cells are fabricated in order to convert sunlight into electrical energy. So the Sun is an ideal light source for demonstrating devices in practical uses. However, testing location, the seasons, environments and the Sun itself are important but uncontrollable factors affecting the solar irradiance in each day or even in a moment during perform a QE measurement. Therefore the measurement in lab scale usually requires artificial light sources that can provide the irradiances similar to the real sun as well as high stability, controllable. The standard solar irradiance employed in photovoltaic technology is defined as AM1.5G, or may be called as 'one-sun', which corresponds to 1000 W/m^2 global averaged power density at the Earth surface.

There are two light sources used in this QE system. A Osram Sylvania EVD 400W halogen lamp was set in the early months and was replaced by an Osram XBO 150W OFR xenon arc lamp latterly. Although the halogen provided very high stability in measurements, it lost much irradiance to environment due to the lamp housing design as shown in figure 21a. On the other hand, better but more expensive

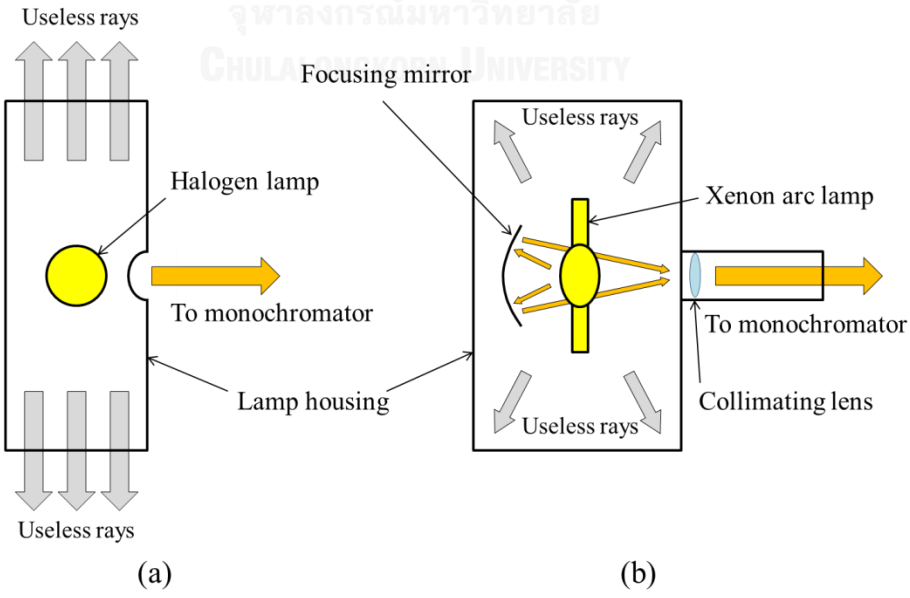

Figure 21 Schematics of the lamp housings for (a) halogen lamp and (b) xenon arc lamp.

light source like a xenon arc lamp was also used. Because the xenon lamp can provide the spectral irradiance close to that of natural sunlight, it is usually used in most solar simulators. The xenon lamp housing was well designed for focusable optical path, so there is small irradiance loss to surroundings in this lamp as shown schematically in figure 21b.

Figure 22 shows a comparison of the spectral irradiances of AM1.5G natural sunlight [37], xenon arc lamp and halogen lamp, which the shape of xenon curve is more similar to the Sun than that of halogen especially in UV and visible regions which carry most of solar energy. Note that the unusual spikes appeared at 320 nm and more than 1150 nm are results from calculating for photon fluxes,

$$\Phi_{ph}(\lambda) = \frac{J_{SC}(\lambda)/q}{\mathrm{QE}(\lambda)}. \tag{15}$$

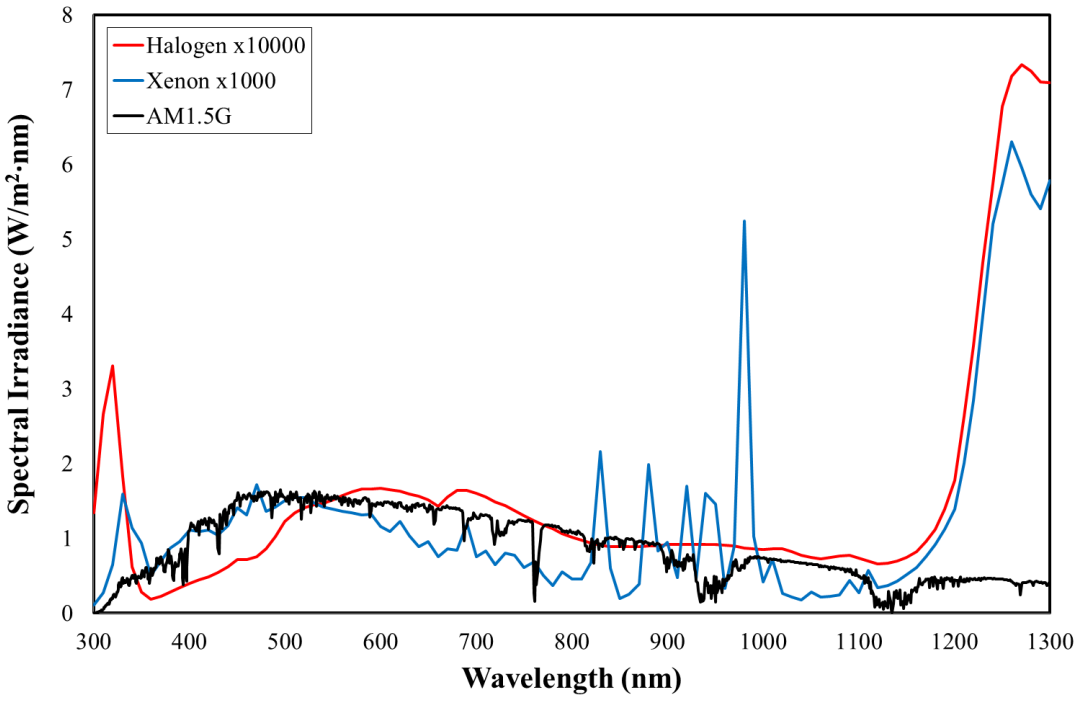

Figure 22 The spectral irradiance of AM1.5G compared to the spectral irradiances of halogen lamp (red) and xenon arc lamp (blue). The multiple of the real values in the inset show that the artificial light sources provide power density much smaller than natural sunlight.

Since values of QE at the absorption edges of QE curves are very small, the photon fluxes and the spectral irradiances $E_\lambda(\lambda)$ at the edges become very large. The spectral irradiances can be calculated by

$$E_\lambda(\lambda) = \Phi_{ph}(\lambda) \cdot \frac{hc}{\lambda} \cdot \frac{1}{\lambda'} \tag{16}$$

where λ' is the given wavelength in unit of $[nm]$. However, the xenon artifact peaks appeared in the infrared and long wavelength regions are still a major problem that need carefulness in measurements using this lamp.

For light path alignment, many QE measurements have dual path configuration where a beam splitter is used; one path for device under tests and another for references. Although the dual path can provide real-time measuring reference data, it requires more space for equipment setup. However, it is possible to design the setup as a simple single path like in our limited space QE system. Therefore devices under tests must strictly be placed in the same position of references (see in figure 24, 25). Additionally, the reference data used for calculating QE results should be calibrated regularly in order to get rid of offsets.

3.2.2 Monochromator

Because QE is defined as a function of wavelength, the system requires monochromatic light to illuminate samples. Monochromator is a device usually set in optic science for separating white light (polychromatic light) into light of different wavelengths. This QE system used a Horiba Jobin Yvon - SPEX500M spectrometer as the monochromator.

A principle rules the light dispersion phenomenon in this monochromator is the wave diffraction from a blazed reflection grating. Consider figure 23, when the saw tooth pattern of a blazed grating diffracts the incident rays A and B of a particular wavelength λ, the constructive interference of outgoing rays A′ and B′ will take place

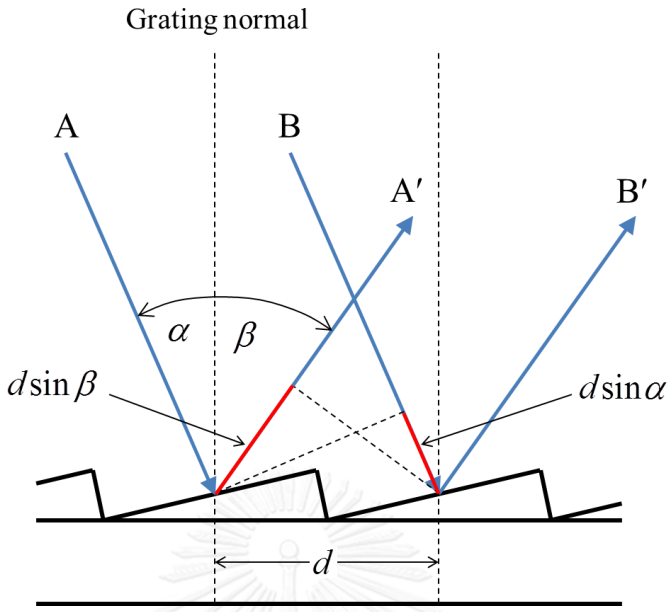

Figure 23 The light rays diffracted from a saw tooth pattern of a blazed reflection grating.

if the path difference between the rays is equal to multiple of wavelength, as described by the grating equation [38]

$$d\left(\sin\alpha+\sin\beta\right)=k\lambda \tag{17}$$

where d is the spacing between two adjacent grooves, which sometime is expressed as the grooves density $n=1/d$. The incident angle α and the diffracted angle β are defined respect to the grating normal. An integer k is the order of diffraction. For the path difference, the first term arises from incidence and the second term results from diffraction.

3.2.3 Reference devices

Since the flux of incident photons cannot be measured in this QE measurement system, the system requires a reference device for calculating the relative QE result of DUT. Although the best reference device so called the first standard is preferred, it is

too expensive and it is not worth to be bought for our system. Therefore the high quality and also high efficiency device should be used as the second standard instead. The high efficiency standard CIGS thin film solar cells calibrated at National Institute of Advanced Industrial Science and Technology (AIST), Japan, are used as the references in this QE measurement.

3.2.4 Current measurement techniques

Source-measure unit (SMU)

The photogenerated current can be measured by basic current measuring units like an amp-meter but automatic working and connectable to computer as well as source-measurement application are not supported in basic instruments. However, those features are available in SMUs. So in many systems, especially I-V measurements usually have the SMU as a tester.

In this QE system, a KEITHLEY 238 High Current Source SMU with four-probe method was applied to measure the current produced by the devices. This SMU was performed using a sweep function for sourcing V (max. value is at ±110.0 V) and measuring I. The 'fast' integration time (416 μsec) was set as default which can provide 4-digit resolution or 10 nA when dealing with measured current of 100 μA. Each point of I-V measurement is normally averaged from 32 readings in order to reduce random noises. Nevertheless, QE measurement requires merely a short-circuit condition. Therefore the SMU was configured to measure I-V characteristics with very small applied voltage bias (such as 2.0 mV). Figure 24 shows a schematic diagram of the QE measurement system with SMU technique.

Lock-in

The lock-in technique was added to this QE system in order to improve the system performance. Since the technique is useful for amplifying very small input signal and also enhancing the signal in high noise situation. Therefore measuring the photogenerated current with lock-in technique is an alternative way for a QE system to acquire high quality data.

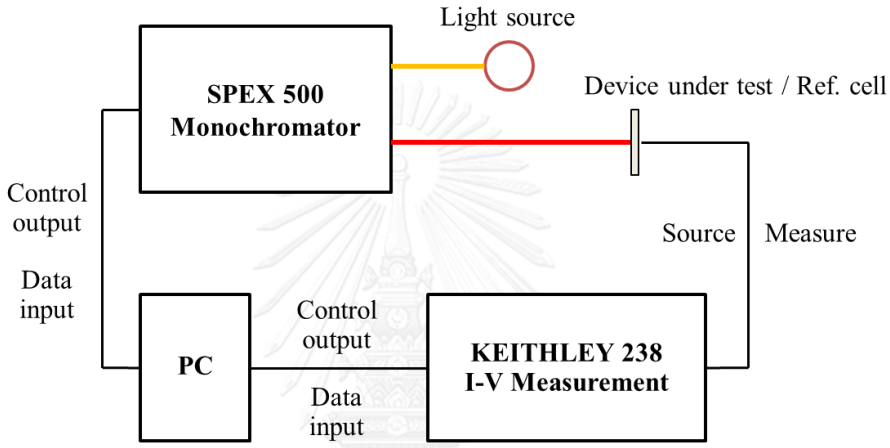

Figure 24 A schematic diagram of the QE measurement system using SMU technique.

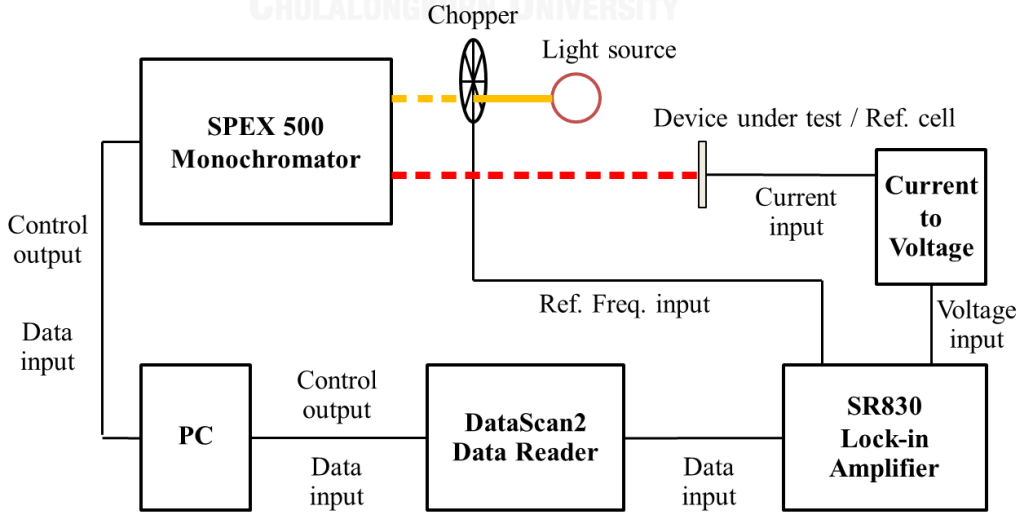

Figure 25 A schematic diagram of the QE measurement system using lock-in technique.

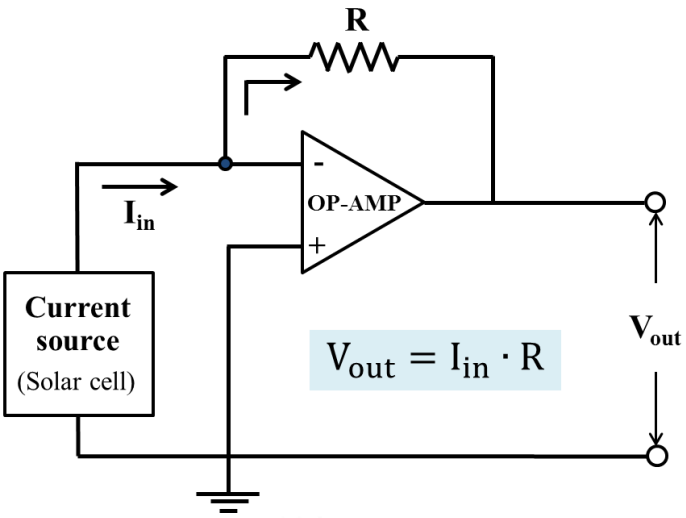

Figure 26 Schematic of current-to-voltage circuit. The order of magnitude of output voltage V_{out} is also amplified from that of input current I_{in} by a gain of feedback resistance R.

The instrument setup of the lock-in technique is schematically depicted in figure 25. An EG&G model 187 light chopper placed between either light source-to-monochromator or monochromator-to-sample is used to chop the continuous photon beam into photon pulses with a constant frequency of 132 Hz. The resulting current pulses produced by a device are then converted into voltage by a current-to-voltage circuit as shown in figure 26. An SR830 DSP lock-in amplifier sequentially reads and selects only the voltage input signals at the corresponding frequency of the chopper. Since the output signal of lock-in amplifier must be amplified not over 10 V or the full scale of the output channel, overall gain and sensitivity should be set properly. At the highest spike of xenon radiation (≈ 9800 Å, see figure 22), the actual photocurrent produced by a cell is generally in order of approximately 0.6 mA is converted into voltage with gain of resistance R = 1000. So, the input voltage of the lock-in amplifier is then about 0.6 V. Next, to prevent the output over full scale, possible gain of the lock-in which is calculated by [10 V/sensitivity] should be 10. Therefore, the sensitivity has to be set at 1 V. A parameter affecting data acquisition so called time constant is fixed at 100 msec. Using proper time constant, the output data becomes more steady and reliable. Before transferring to computer, the data are converted from analog into digital by DataScan2.

In addition, to make one easily understand how the lock-in technique measures photogenerated current, the concept is described by figure 27. First of all, we assume the input signal of a lock-in amplifier is the pulsed voltages that are already converted from current to voltage by an op-amp circuit. On the other side, the frequency of the chopper is used as the reference frequency in lock-in amplifier. The input signal is then read and selected only at a specific frequency, so the resulting signal likes a multiplied combination of the input and reference signals. If one let these two signals in phase, the result contains all of input signal. Conversely, the result will be vanished if the sources are 90° out of phase. After that, the sum signal is converted into output signal by

$$V_{output} = \frac{\int_0^T V_{sum}\,dt}{\int_0^T dt} \tag{18}$$

where the denominator is added for normalization. Finally, the output dc voltage signal is then transferred to the analog-to-digital converter (ADC) and PC consecutively. As one has seen, the step of selecting input signal corresponding to the reference is an important part of lock-in technique. If there are noises generated randomly by environment, noises will not be included in the result. Therefore, the higher quality data will be obtained.

An issue involving with measuring current by the lock-in technique has to be discussed here. Since a low noise inverting op-amp 07 was used in the current-to-voltage circuit, the output signal is thus 180° out of phase with the input. This may affect the results of voltage bias conditions (section 4.4). However, this problem can be neglected because the current produced from solar cells is direct current and the lock-in amplifier is always set input and reference signals in phase. Therefore, increasing or decreasing in photocurrent collection by voltage bias is then directly exhibited.

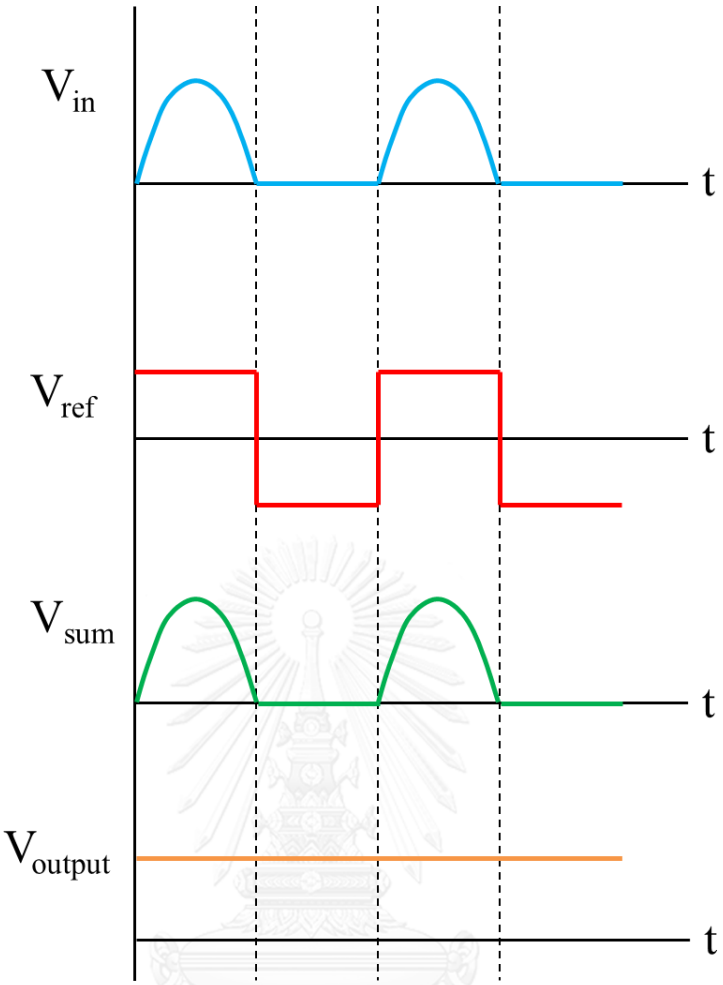

Figure 27 Signals measured and calculated in the lock-in technique.

3.2.5 Reliability of spectrometer

The tests of accuracy and reliability of the QE system should be performed before using in practice. By an advantage of characteristic spectrum of sodium lamp, the dominated well-known doublet so-called the Sodium D-lines at 5889.950 Å and 5895.924 Å should be detected and resolved. Figure 28 shows the photoresponse, or photogenerated current as a function of wavelength, to the sodium spectrum using a mono-crystalline silicon solar cell as a detector. There are two peaks appearing at approximately 5890.0 Å and 5896.0 Å. The peaks are broadening when the entrance and the exit slit widths are wider as expected. Narrower slit widths yield better

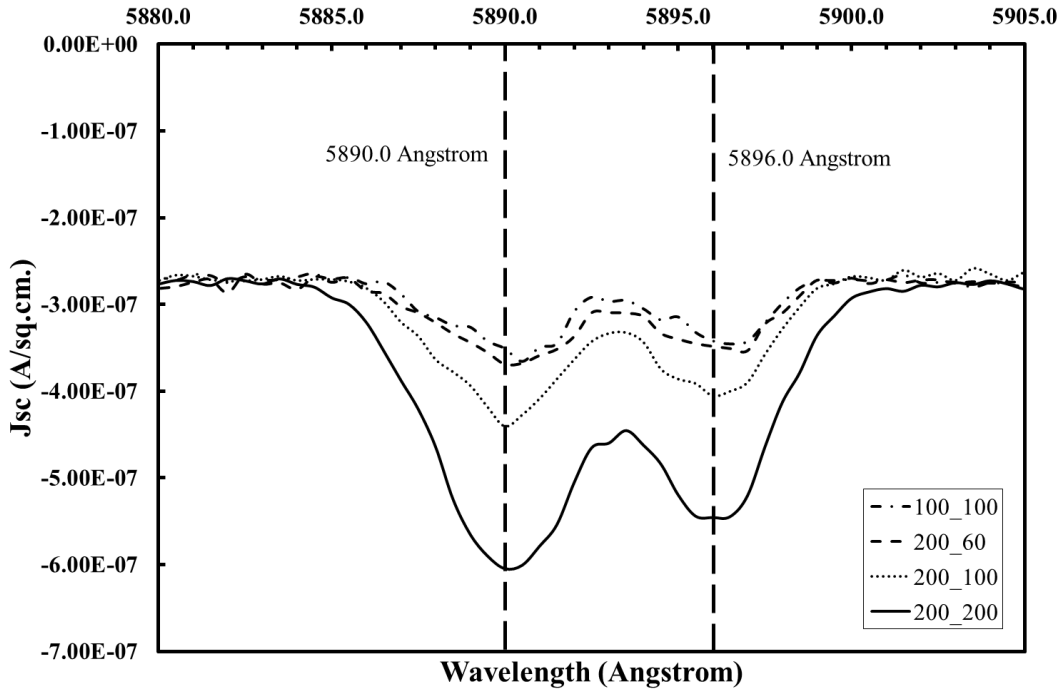

Figure 28 A comparison of the photoresponses of a mono-crystalline silicon solar cell to the sodium spectrum with various slit widths. Numbers labeled in the inset indicate to the widths of entrance slit and exit slit (in μm), respectively.

resolution but lose the light intensity. So they could not be used to observe a photoresponse of a solar cell due to limited ability to produce the photocurrent from very small incident flux, unlike a high efficiency photodetector.

3.3 Control program

The controlling program is an important part of the system because it is used to control the automatic workings, calculate QE results as well as data storing. The monochromator and current measuring units are connected to a computer via RS-232 and GPIB interfaces. The graphical data flow programming software named 'Agilent VEE' is used for writing set of direct I/O commands, calculating and exhibiting the results.

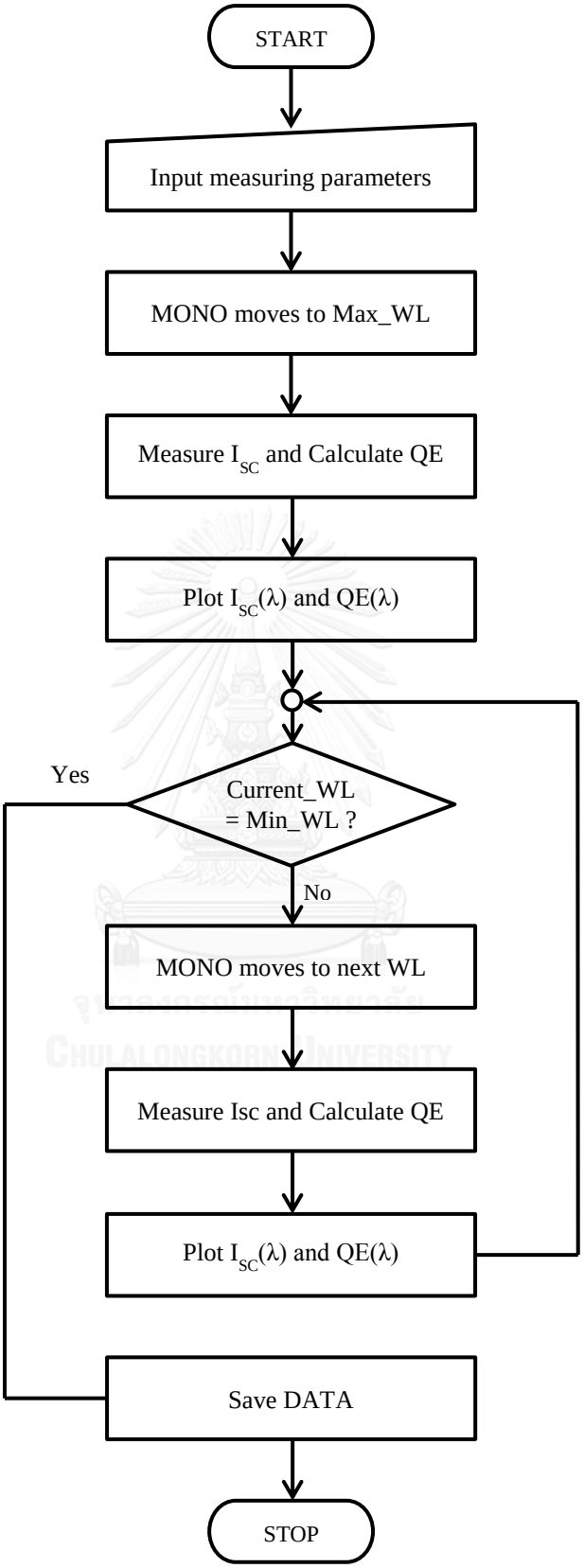

Figure 29 Flow chart of the QE system showing the whole concept of the QE measurement.

3.3.1 The flow chart

Although the whole QE system was governed by many sets of complicated coding comprising the controlling program, the concept is still based on the fundamental of QE measurement which can be designed as a flow chart shown in figure 29. All of measuring parameters are required at the beginning. After that, the essential equipment such as monochromator and current measuring units are performed corresponding to their received commands. At each step of the grating motor, the produced current is measured and is then used to calculate QE of the device under test. Here, a 'for' loop is written to govern "pause → measure → step" loop working. Note that the monochromator is commanded to scan from maximum to minimum wavelengths in order to increase the photon energy as the wavelength decreases.

3.3.2 Coding in Agilent VEE

In a VEE program, all commanding codes are designed to contain in VEE objects. The objects can be connected together via their pins which govern the sequences of execution and the data flow. Figure 30 demonstrates an example of a VEE program for calculating A*A, where A = 0, 1, 2, …, 10, and then plotting between A and A*A. As one has seen, programming with VEE provides ready-to-use functions, so reducing complexity, and give convenience in graphically result exhibition.

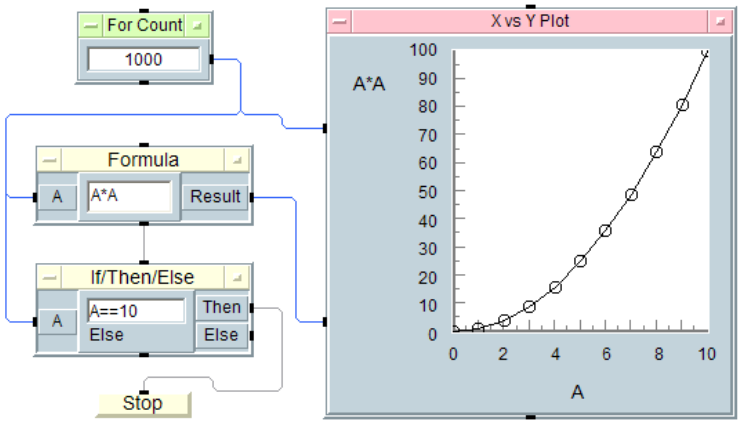

Figure 30 An example of VEE program.

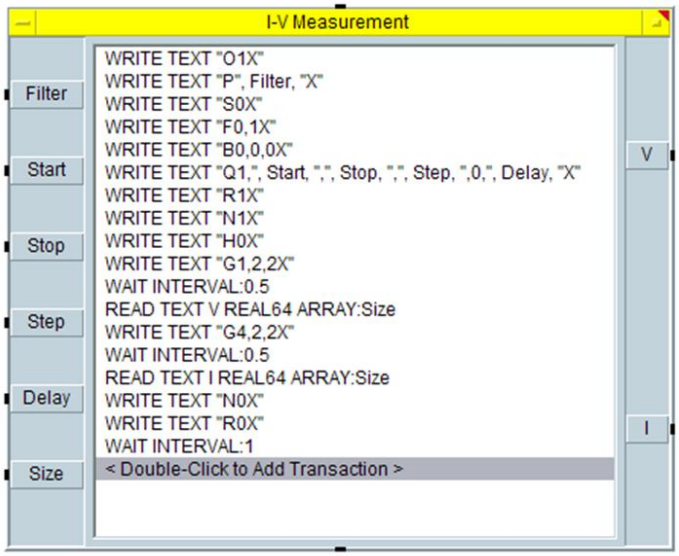

Figure 31 A set of direct I/O commands for configuring an I-V measurement.

To control instruments, the direct I/O commands have to be written and then directly transferred through the connected interfaces. They must conform to the commands described in instruction manuals of each instrument. Figure 31 exemplify a set of direct I/O commands for performing an I-V measurement.

3.3.3 Controlling by users

Any good program for measurements should be designed with user-friendly. Therefore, this QE system provides users a main monitor for setting the instruments and also observing the results. Figure 32 is the main screen for the QE measurement using SMU technique. User can conveniently configure the measuring parameters on the left part. During a measurement, real-time results of the photogenerated current and the EQE as a function of wavelength will be plotted graphically in the middle of the screen. Red and blue curves in the plots exhibit the REF data and the DUT results, respectively. Besides EQE curves, the photoresponses, the small biased I-V characteristic as well as numerical results are also displayed.

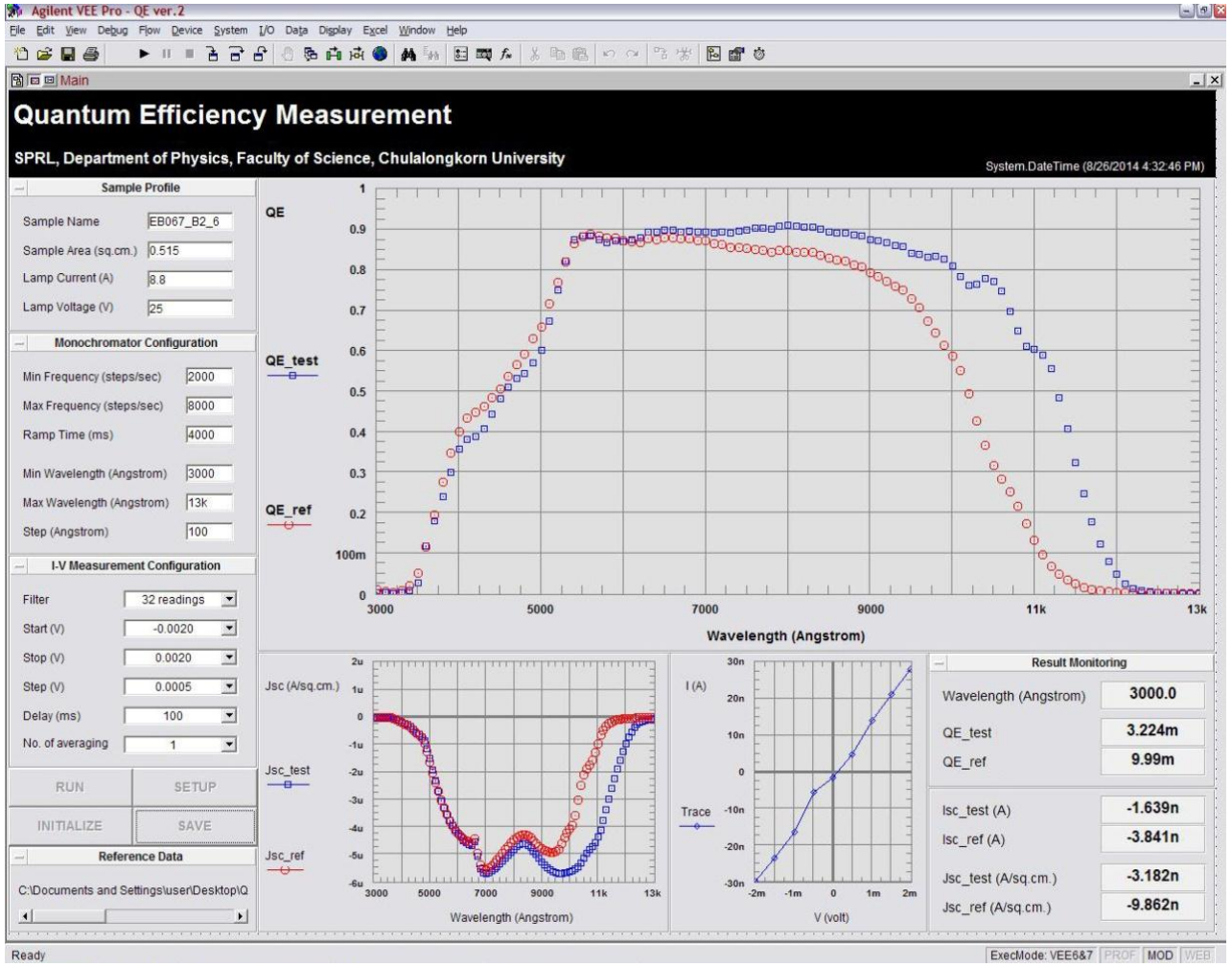

Figure 32 Main monitor of the QE measurement system designed for users.

CHAPTER IV

INVESTIGATING PHOTORESPONSES BY QE MEASUREMENTS

4.1 Varying deposition conditions of CIGS

4.1.1 Devices and characterization

In this study, the CIGS-based thin film solar cells were fabricated by the standard 3-stage fabrication techniques. Each thin film layer in all devices was deposited by the same conditions except for the absorber layer as shown in table 1.

To study the effect of various growth conditions on solar cell performances, the elemental compositions in the CIGS absorbers were investigated by the energy dispersive x-ray spectroscopy (EDS) for the composition depth profiles. After completing the cell fabrications, those devices were measured for their J-V characteristic curves and the energy conversion efficiencies using a xenon arc lamp illumination under AM1.5G condition. Finally, QE measurements were performed to analyze the photogenerated current collections for each growth condition.

4.1.2 The composition depth profiles of CIGS

A depth profile yields the details of distribution of constituent elements in the CIGS as a function of depth from the front surface. Since $CuIn_{1-x}Ga_xSe_2$ is an alloyed semiconductor, its bandgap energy depends on an elemental composition ratio, $x = [Ga]/([In]+[Ga])$. This means a depth profile implies the detail of the bandgap energy at various depths which is an important information in bandgap engineering.

Although thin solid films are generally analyzed the elemental composition for depth profiles by the secondary ion mass spectroscopy (SIMS), the EDS technique can also be employed in qualitative investigation. By scanning the cross section of a sample as shown in figure 33, the constituent elements will be analyzed.

Table 1 Details of the deposition conditions of each device.

Device	Absorber layer(s)
A	CIS
B	CGS
C	CIGS
D	CIS/CGS
E	CGS/CIS
F	CGS/CIS/CGS

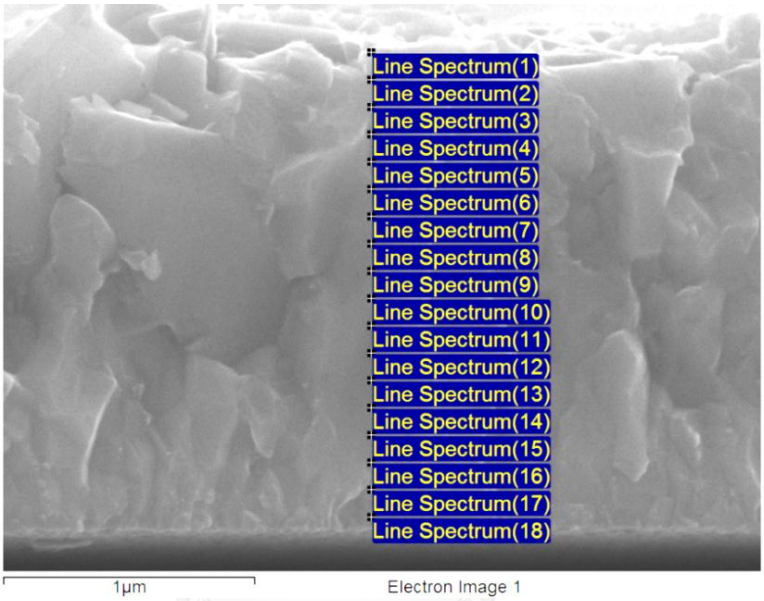

Figure 33 Cross section SEM image of a CIGS/Mo/SLG sample showing the line spectra of the EDS analyzed points for obtaining a composition depth profile.

The compositional depth profiles of CIGS absorbers for different deposition conditions are shown in figure 34. The horizontal axis indicates the distance from the front surface of the absorber layers. Note that the samples in this EDS analysis just the CIGS-based thin films deposited on Mo back contact. For the results of mono-layer absorbers (samples A, B and C), the composition ratios are constant at x = 0, 1 and 0.25, respectively. Their results are not shown here because sample C, which is a complete device used as reference in QE measurements, is not characterized by this destructive technique. On the other hands, graded bandgap energies are found in bi-layer and tri-layer (sample D, E and F) due to the non-uniform distribution of Ga in absorber layers. The distributions show continuous inclined shapes not the discontinuous steps because of the diffusion of Ga and In during deposition processes.

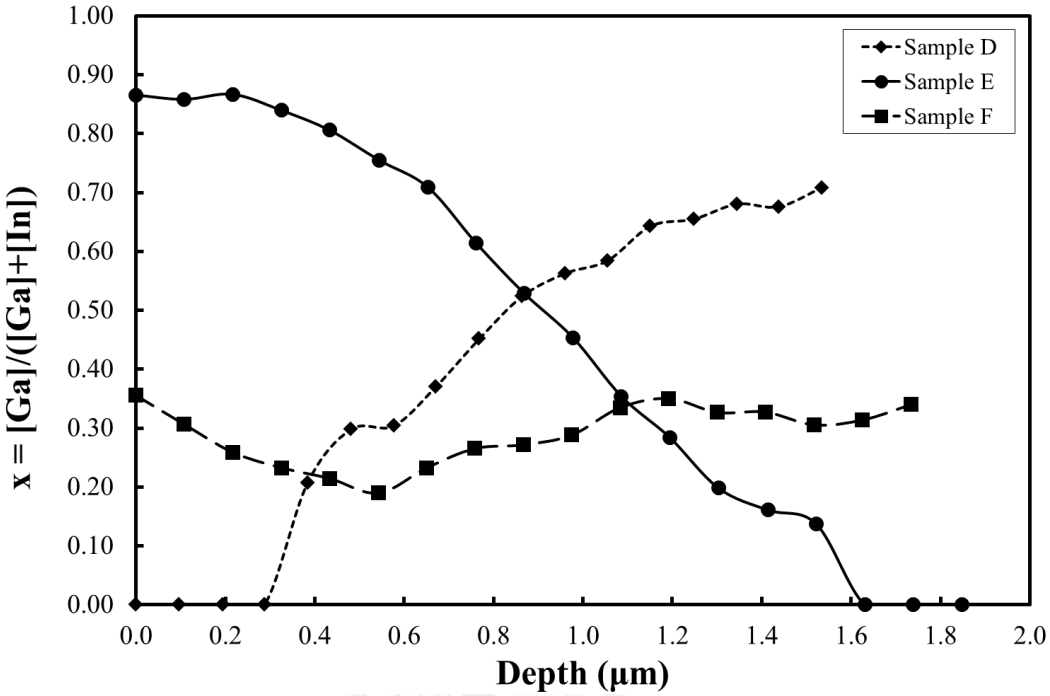

Figure 34 The depth profiles of the CIGS absorber layers of sample D, E and F.

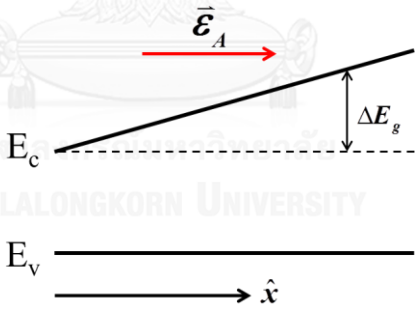

Figure 35 Normal graded bandgap and the additional electric field.

However, with the presence of the bandgap grading, the gradient of potential energy causes the additional electric field $\vec{\varepsilon}_A$ inside the absorber layer as depicted in figure 35. The fields can be described by

$$\vec{\varepsilon}_A = \frac{1}{e}\frac{d\left(\Delta E_g\right)}{dx}\hat{x} \tag{18}$$

where e is the electronic charge, x is the distances from front surface and ΔE_g is the bandgap energy modification. By applying suitable bandgap grading, the additional field can enhance the photogenerated current collection and the conversion efficiency of solar cells by increasing the diffusion lengths and reducing the recombination rates of the carriers.

According to the depth profiles, sample D and E show single gradings, having back surface field (normal grading) and front surface field (reverse grading). Conversely, double grading type consisting of a minor reverse and a dominant normal grading is exhibited in sample F.

4.1.3 The photovoltaic parameters

To demonstrate solar cell performance, the short-circuit current density (J_{SC}), the open-circuit voltage (V_{OC}), the fill factor (FF) and the total conversion efficiency (η) were measured by J-V measurements under AM1.5G illumination. We note here that the area of each solar cell is 0.515 cm^2. Table 2 and figure 36 exhibit the results and also the characteristic curves.

According to the results of mono-layer absorber, device A can produce highest photogenerated current J_{SC} due to its narrowest bandgap energy. On the contrary, the widest bandgap device B can absorb only high energy photons, so it contributes smallest current generation. The effect of bandgap grading on photocurrent collection is clearly found in device D and E. By an influence of the back surface fields, the photogenerated minority carriers in device D are swept away from the recombination center at the back contact and they are also driven to cross the p-n junction easily. While the reverse fields in device E act as a very high barrier for carriers to overcome and cross the junction or even to diffuse in the bulk region. So device E can produce smaller J_{SC} than device D. In case of V_{OC} , since it relates to bandgap energies of the absorbers, device B and E thus has very high V_{OC} . However, too narrow bandgap or too low V_{OC} is not beneficial to solar cells because the photogenerated carriers tend to

Table 2 The photovoltaic parameters of each device.

Device	Absorber layer(s)	J_{SC} (mA/cm^2)	V_{OC} (mV)	FF (%)	η (%)
A	CIS	42.49	431	54.07	9.90
B	CGS	9.83	812	51.48	4.12
C	CIGS	28.59	655	69.79	13.07
D	CIS/CGS	32.97	559	70.00	12.90
E	CGS/CIS	14.39	755	49.20	5.35
F	CGS/CIS/CGS	35.75	592	72.80	15.41

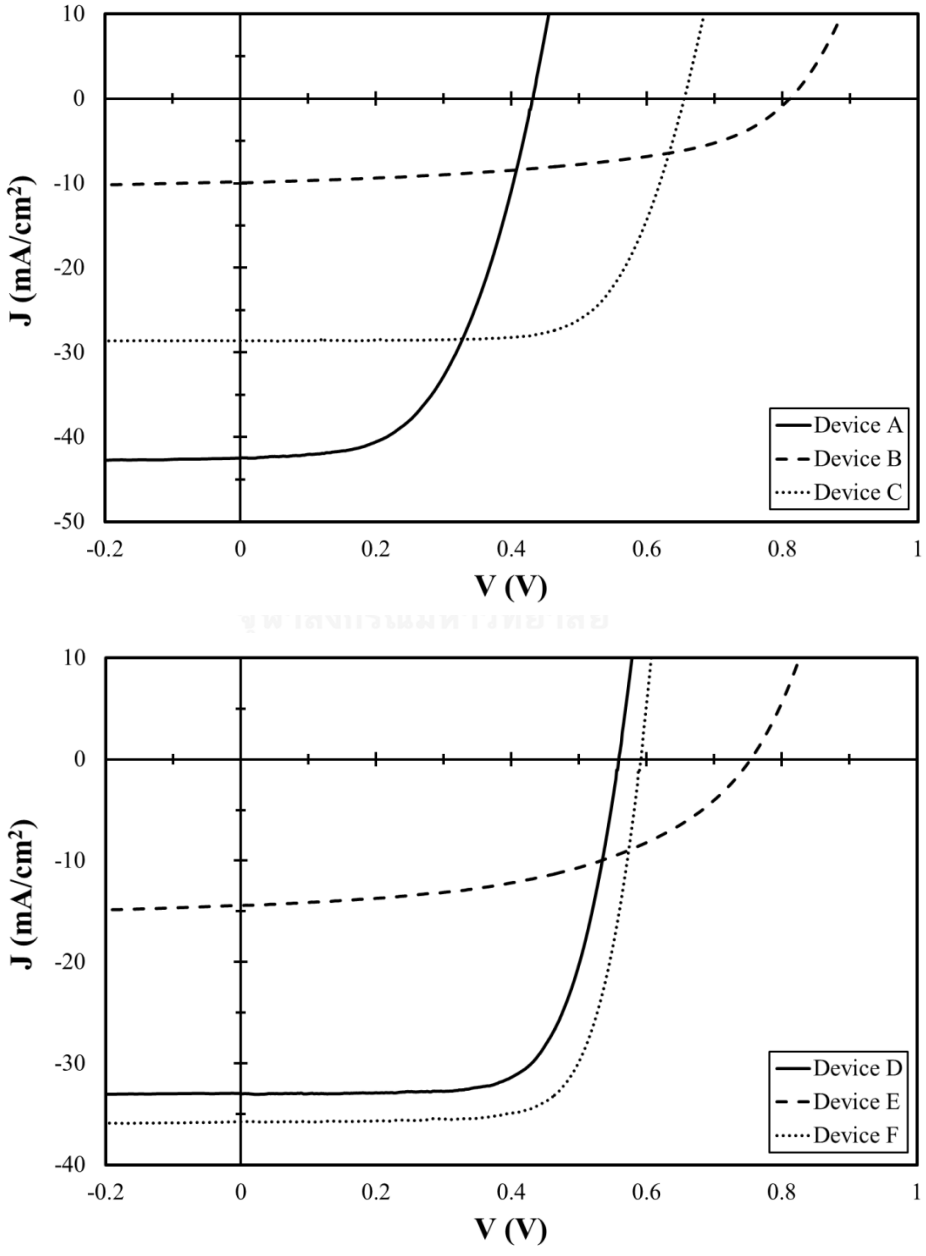

Figure 36 The J-V characteristic curves of each device.

be recombined before delivered to external circuit. Therefore, the uppermost CGS thin layer in device F is deposited in order to reduce the rate of recombination at the CdS/CIS interface in device D. In other words, it is grown to increase the V_{OC} parameter. This modification then achieves the best device where all parameters are enhanced.

In addition, these results imply a fact that high collected current does not affirm high power output. Since the conversion efficiency η yields the efficiency to convert photon energy into maximum electrical power, thus, good solar cells should have suitable trading between J_{SC}, V_{OC} and FF as seen in devices C, D and F. Moreover, this can be used as a feedback information for the deposition of the CIGS absorber layers. The advantage of the double grading absorber is that the thinner absorber can be obtained while maintaining the level of acceptable efficiency.

4.1.4 The external quantum efficiencies

The EQE curves of CIGS thin film solar cells are shown in the figure 37. The results of the EQE and the solar cell parameters in table 2 are in good agreement. The integrated areas under EQE curves imply the overall photogenerated currents that solar cells can produce to external load. The absorption edges at the long wavelengths indicate the beginning of the photon absorption, so correspond to the bandgap energy of the absorber and thus affecting V_{OC}. And since these solar cells were fabricated by varying only absorber layers, the EQE values for wavelengths shorter than 5000 Å which the absorptions in CdS buffer layer ($E_g \approx 2.4$ eV) and i-ZnO and ZnO(Al) window layers ($E_g \approx 3.2$ eV and 3.5 eV, respectively) take place are about the same.

For the device A with narrowest bandgap energy, the photon absorption begins at approximately 12000 Å, while the absorption in device B and C (x = 0.25) start at approximately 7500 Å and 11000 Å, respectively. It can be seen that when the bandgap energy of the mono-layer absorber increases, the photogenerated current then decreases. In cases of bi- and tri-layer absorbers, the total collections of photocurrent are influenced by bandgap grading as discussed in the cell parameters results.

There is an interesting issue in comparing EQE between device D and F. For low energy photons of wavelength longer than 8500 Å, device F can produce more collectable currents than device D because the averaged bandgap of the first one is narrower. Conversely, for wavelength shorter than 8500 Å, the averaged bandgap of

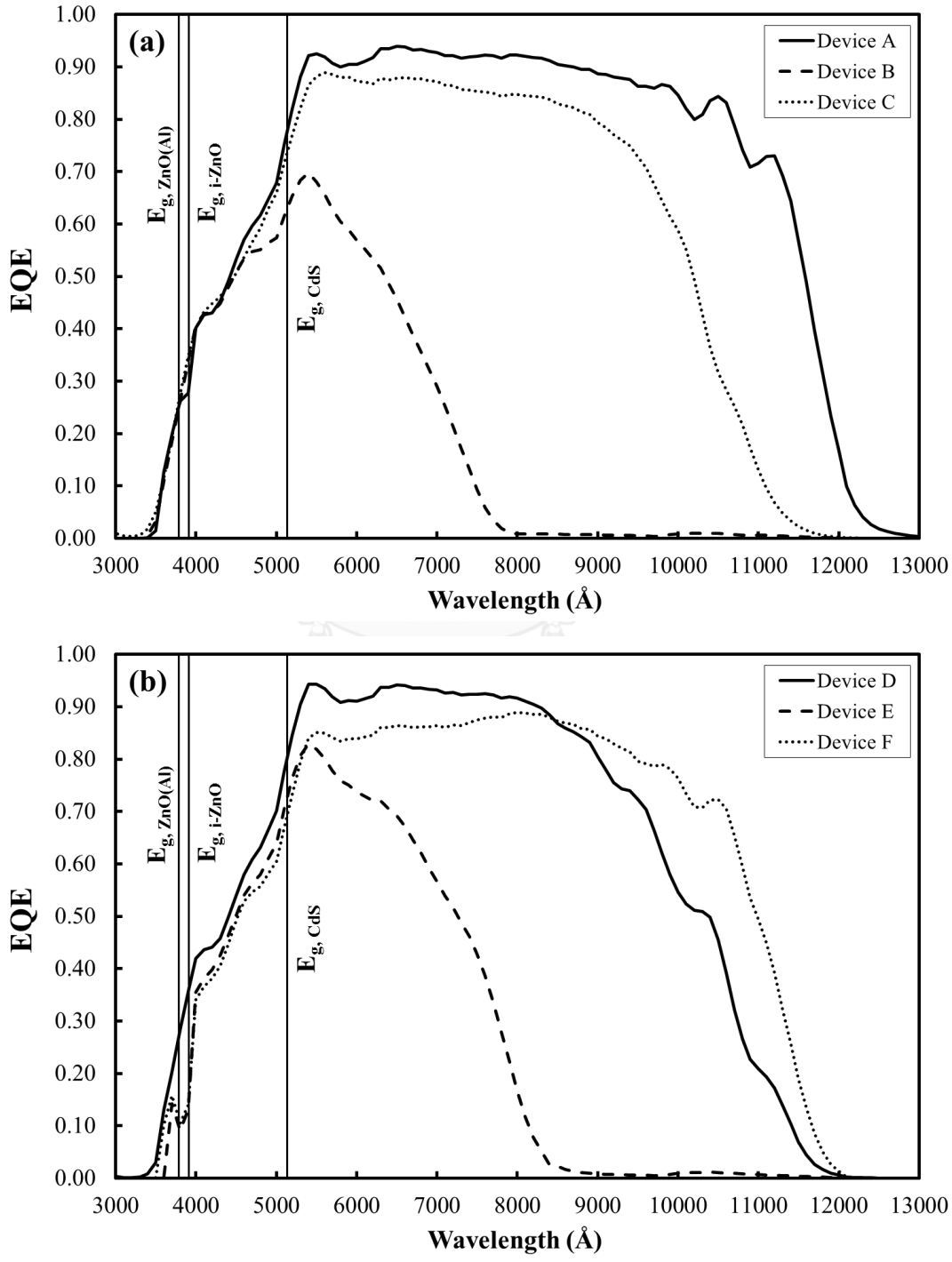

Figure 37 The external quantum efficiency curves.

normal graded device rather matches to the high photon energies, thus resulting to significantly improve in photogenerated current collection. However, it has to be noted that these growth conditions are in a study of mono-, bi- and tri-layer absorber depositions and they are not generally used in the real bandgap engineering. Therefore, the conditions may not provide high efficiency devices as reported in other works [39-41].

As one has seen, not only results of the composition depth profiles, the photovoltaic parameters and the external quantum efficiencies are in good agreement, but also the detailed information of photogenerated current are revealed. This also shows an advantage of using QE measurements.

4.2 Identifying defective devices

To clarify about the current collection in solar cells, the current leakage is needed to be included into consideration. The current leakage can occasionally be observed in the J-V characteristic curves. It is a problem arising from the defective p-n junction at the CdS/CIGS or i-ZnO/CdS interfaces. When the leakage occurs as depicted in figure 38, the photogenerated carriers are likely to cross the junction and recombine through this leakage path. This means a solar cell cannot deliver those carriers to external circuit and then lead to a loss in photogenerated current.

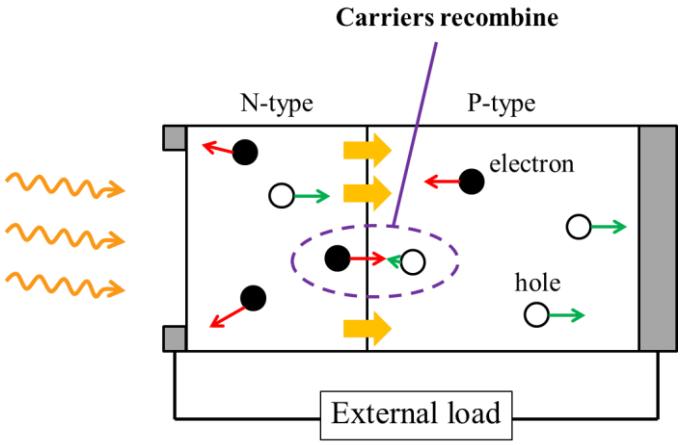

Figure 38 Loss of carriers by current leakage in a defective p-n junction solar cell.

Besides the four photovoltaic parameters as discussed in the previous section, the resistances are also calculated for a J-V characteristic curve. Because the inverse of a slope in J-V curve yields a characteristic resistance, a practical solar cell with one junction usually has two resistances that dominate in different voltage biases. As mentioned in section 2.3.1, the series resistance accounts for the resistance of current paths in layers and contacts, while the shunt or parallel resistance usually refers to resistance of small parallel paths through or around the device layers. This implies that the current leakage problem which relates to defective p-n junction directly involves with the shunt resistance. In addition, it is preferred to have large shunt resistant and small series resistant for a good solar cell.

Table 3 shows details the series and shunt resistances of three CIGS solar cells calculated from the J-V characteristic curves in figure 39. From the results, device G that has small R_S and very large R_{SH} is the best efficient cell compared to other two devices. The smaller series resistance of device H compared to device G implies the higher collectable photogenerated current. But the current loss by leakage may also occur as the shunt resistance is much smaller. So the current collection in device H is thus smaller. For the worst efficient device I, large R_S and small R_{SH} result to the smallest photocurrent and also the conversion efficiency. Note that these cells are three sub-cells with area of 0.515 cm^2 in the same 3x3 cm^2 device. They were fabricated by the same deposition conditions. So slightly differences in solar cell parameters are generally observed and can be thought as the effect of thin film uniformity during fabrication.

Table 3 The cell parameters include the series resistance R_S and shunt resistances R_{SH} of three CIGS solar cells.

Device	J_{SC} **(mA/cm^2)**	V_{OC} **(mV)**	***FF*** **(%)**	η **(%)**	R_S **(Ω·cm^2)**	R_{SH} **(Ω·cm^2)**
G	29.57	678	71.00	14.24	0.75	2876
H	28.95	667	65.21	12.59	0.46	614
I	28.46	656	64.07	11.96	1.08	314

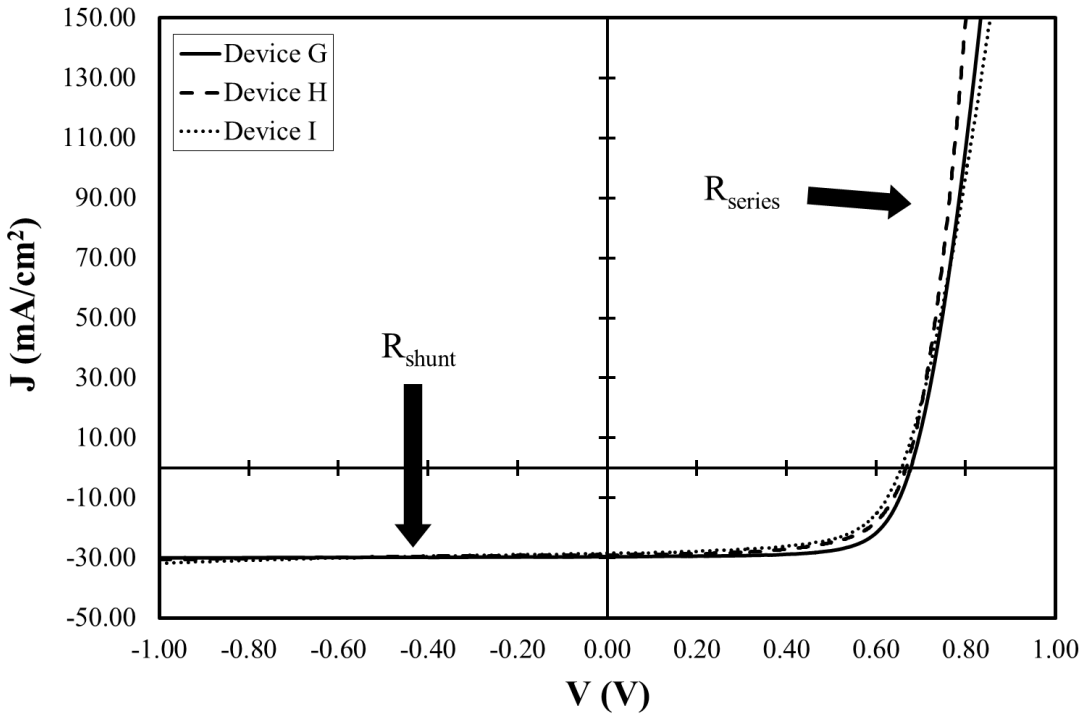

Figure 39 The J-V characteristic curves of device G, H and I.

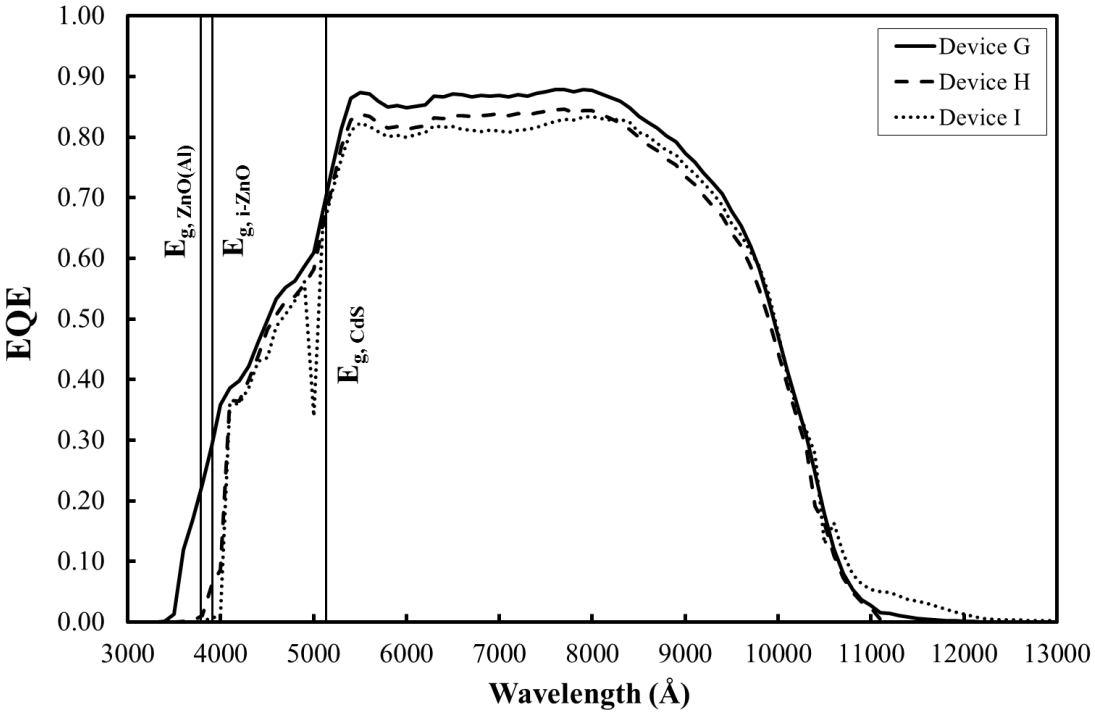

Figure 40 The EQE curves of device G, H and I.

J-V results may imply existence of the current leakage but they are not enough to identify the causes of problem, such as, which thin film layers or which interfaces have the defect. By using the QE measurements, the results raise some interesting issues involving the leakage problem. Figure 40 shows the EQE curves of the three CIGS solar cells exhibiting the difference in their photogenerated current collections. The difference is relatively easy to observe especially at the short wavelengths. There are sharp drops in EQE of the worst device I appearing at approximately 4000 Å and 5000 Å, corresponding to the energy of 3.10 eV (near bandgap energy of i-ZnO) and 2.48 eV (near bandgap energy of CdS), respectively. While only sharp drop at 4000 Å is observed in device H. Since the EQE for wavelengths shorter than 5000 Å indicate the current collectability of the combinations of CdS, i-ZnO and ZnO(Al). If these abruptly decreases indicate the current loss in the small shunt resistant devices, this means the ZnO(Al)/i-ZnO window layers and the CdS buffer layer cause some problems that lead to the defective p-n junction at the CIGS interface. To confirm the occurrence of these sudden decreases, EQE measurements were repeatedly performed many times as well as other solar cells were characterized. The results show the current loss, for example, as shown in device E and F in figure 37b, and a relation between device resistances and sharp drops is not coincidence. This investigation is another advantage of using QE measurements.

4.3 SMU and lock-in techniques

Noise becomes a significant problem when measuring signals are very small like in QE measurements. In case of using xenon arc lamp as a light source, the noisy xenon characteristic irradiance affects the smoothness of data. As described in section 3.2.4, the SMU and lock-in techniques are current measuring techniques used in this QE measurement system. The first technique is performed to measure the photogenerated current at the short-circuit condition and the data obtained from this method are the actual current. Conversely, the latter technique is used to amplify the signal over noised backgrounds by measuring pulsed photocurrent at a particular frequency. So the resulting data are the amplified current. Therefore, a comparison of

the EQE results obtained from these two techniques should be done to confirm an assumption that the lock-in provides smoother data acquisition.

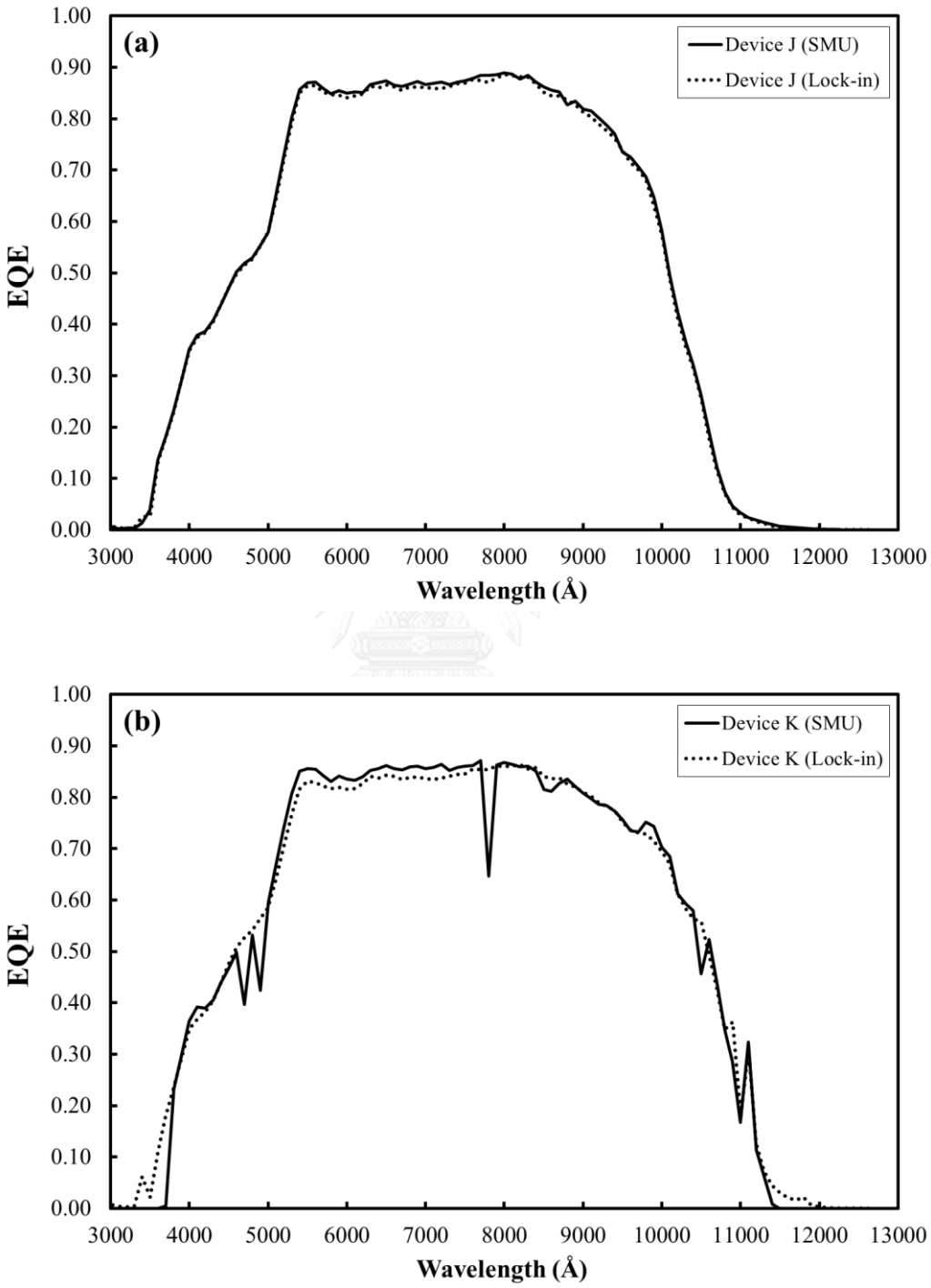

Figure 41 Comparisons of the EQE curves of device J and K obtained from SMU and lock-in techniques.

Figure 41 show the EQE comparison between results obtained from SMU and lock-in techniques. The devices used in this comparison are CIGS thin film solar cells where device J is a good junction solar cell while device K is a rather poor defective junction cell. In case of device J in figure 41a, it is difficult to choose the better method because the two results are very close to be overlapped, although, little offset due to device positioning causes a bit lower in the EQE values of the lock-in. On the contrary, device K as shown in figure 41b shows clearly different between the two results. Many little spikes and dips, which are thought as an impact of xenon characteristic peaks and noised backgrounds, are found when using the SMU. Whiles the much smoother results could be obtained from the lock-in technique. This EQE comparison thus exhibits a better point of the lock-in technique over the SMU. Moreover, shorter in the overall measuring time per one test taken for the lock-in method (~ 30 minutes) than that of the SMU technique (~ 45 minutes) is another advantage for improving this QE measurement system.

4.4 Voltage bias

In the QE measurement, solar cells are usually measured at the short-circuit condition where a voltage drop across device is zero. Nonetheless, the solar cells in practice generally operate at certain voltages and currents depending on the resistances of external loads. So it will be advantage if the photocurrent collection can also be investigated at more realistic condition. To do this, the biased voltages were sourced to solar cells at various levels as well as the photocurrents were measured. Note that this experiment employed the SMU technique for convenience in source-measure configurations and the halogen bulb for high stable photon fluxes.

Figure 42 shows the EQE curves of a CIGS solar cell with various bias voltage levels. Zero bias denotes the normal or un-bias condition while 0.2 mV, 0.5 mV and 1.0 mV were biased in both forward and reverse configurations. Note that the levels of voltage bias applied in this study are rather very small when compared to the maximum power point voltage V_{MP} of J-V measurement (~ 400 mV). Since the

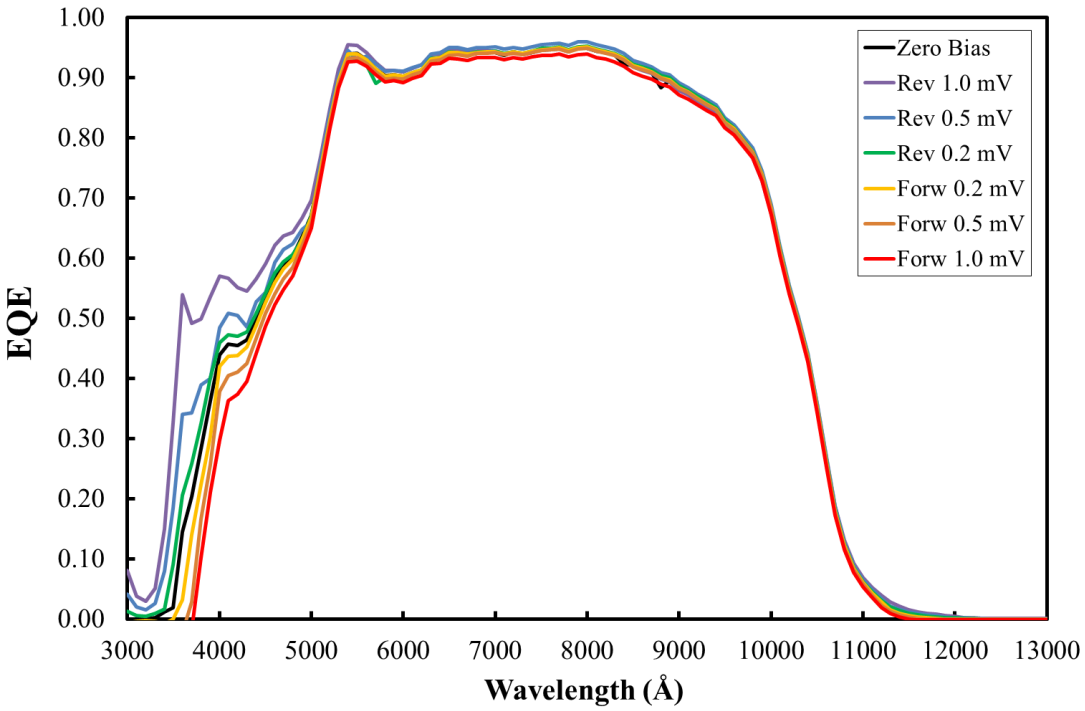

Figure 42 The EQE curves of a CIGS solar cell with different voltage biases.

incident photon intensity in the QE measurement, especially using of halogen bulb, is much lower than AM1.5G illumination (approximately 10,000 times lower, according to figure 22). Therefore, the V_{MP} in J-V curves of each photon wavelength in QE measurement averaged in order of millivolt do make sense.

According to the EQE curves, all results superpose at the long wavelength absorption edges and then become slightly different in the top flatted EQE region. The effect of voltage bias on EQE is clearly exhibited for short wavelength photons where the CdS buffer layer and ZnO window layers generate photocurrents. This can be explained by the energy band diagram of a p-n junction in figure 13. When non-zero voltage is applied to the electrodes of a cell, the majority carriers in each region will respond to this external stimulation by moving according to the potential gradient. In case of forward bias, the drifting of holes in p-type and electrons in n-type toward the junction causes recombination between the moving carriers and the carriers forming the SCR. This carrier annihilation process results in a narrowing of the SCR. Conversely, the drifting of carriers outwards from the junction in case of reverse bias

thus leads to wider of the SCR. The width of SCR affects the photogenerated current collection, particularly near the p-n junction. Therefore, the cell with reverse voltage biases thus produce higher numbers of carriers compared to zero bias because of wider SCR. Whiles the photocurrent can be collected in smaller number in forward voltage biases due to narrower width of SCR. However, one has to note that only forward bias can take place when external load is connected in a solar cell in a practical operation. Although smaller number of photocurrent is generated, solar cells operate best at its maximum electrical power condition; $J_{MP} \times V_{MP}$.

CHAPTER V

SUMMARY

This thesis has been presented the fundamental principles of a photoelectronic characterization technique called quantum efficiency (QE). The theoretical backgrounds, especially the solar cell operation and the QE measurement have been introduced. More detailed information about the photogenerated current revealed in QE result is the most important advantage of using QE measurement to study the photoresponse of photovoltaic devices.

For the first main part of this work, a quantum efficiency measurement system was constructed based on the concept of instrument setup described in chapter III. The ways to improve the system performance were also discussed. In addition, this QE measurement system was designed as automatic characterization that can be controlled via the controlling programs written in VEE software.

For another part, the QE measurement system was employed to investigate the photogenerated current collection of the $CuIn_{1-x}Ga_xSe_2$-based thin film solar cells as summarized in follows:

- The CIGS solar cells with different deposition conditions of the absorber layer were characterized by the QE measurement together with the current density-voltage (J-V) measurement and the energy dispersive x-ray spectroscopy (EDS). The composition depth profiles exhibited the bandgap grading in the bi- and tri-absorber layer devices. The results of J-V and EQE then showed the influence of bandgap profiling on the collections of photocurrent and other solar cell parameters. Their results are in good agreement. So this is a point confirming successfully working of this new QE measurement.

- Not only the good devices were studied, the defective solar cells of poor performance were also investigated by this QE measurement in order to identify the causes of problem. The QE results showed the abrupt losses of the photocurrent collection at approximately 5000 Å and 4000 Å where correspond to the photon absorption in CdS buffer layer and ZnO window layers. This observation thus implies that the CdS/CIGS and ZnO(Al)/i-ZnO/CdS interfaces may cause some problems that lead to the current loss in defective devices.

- Replacing halogen lamp with xenon arc lamp provides better matching of spectral irradiances between the artificial light source and the natural sunlight. But the QE system then faced noisy problem due to xenon characteristic irradiance. Therefore, the lock-in technique which usually contained in most measurements dealing with small signal and high noise backgrounds was then applied to the system. The comparison between SMU (basic technique) and lock-in (new technique) exhibited smoother data acquisition of the latter technique. The yield from this small experiment is a way to improve performance of this QE measurement system.

- Voltage bias is a configuration sourcing voltage to the solar cell electrodes in order to demonstrate solar cell performance in practice. The EQE curves show clearly the effect of the bias on photogenerated current at the wavelengths corresponding to ZnO/CdS/CIGS interfaces or p-n heterojunction. The results can be thought that reverse bias widens the space-charge region width, so the photogenerated current collection increases. Whiles the opposite trend is observed in forward bias. That means solar cells in practice that connected with external load narrow their space-charge region width, resulting in the reduction of the photocurrent collection.

REFERENCES

1. Morton, O., *Solar energy: A new day dawning?: Silicon Valley sunrise.* Nature, 2006. **443**(7107): p. 19-22.
2. BBC. *History: Archimedes*. 2002 [cited 2015 20/1/2015]; Available from: http://www.bbc.co.uk/history/historic_figures/archimedes.shtml.
3. Becquerel, A.E., *Mémoire sur les effets électriques produits sous l'influence des rayons solaires.* Comptes rendus de l'Académie des Sciences, 1839. **9**: p. 561-567.
4. Williams, R., *Becquerel Photovoltaic Effect in Binary Compounds.* The Journal of Chemical Physics, 1960. **32**(5): p. 1505-1514.
5. Smith, W., *Effect of Light on Selenium During the Passage of an Electric Current.* Nature, 1873. **7**: p. 303.
6. Adams, W.G. and R.E. Day, *The Action of Light on Selenium.* Philosophical Transactions of the Royal Society, 1877. **167**: p. 313-349.
7. Fritts, C.E., *On a New Form of Selenium Photocell.* American J. of Science, 1883. **26**: p. 465.
8. Perlin, J., *The Silicon Solar Cell Turn 50*, NREL, Editor. 2004, Perlin, J.: NREL - Education Resources.
9. Ohl, R.S., *Oral-History: Russel S. Ohl*, F. Polkinghorn, Editor. 1975: Center for the History of Electrical Engineering, The Institute of Electrical and Electronics Engineers, Inc.
10. Ohl, R.S., *Light-sensitive electric device*. 1946, Google Patents.
11. Chapin, D.M., C.S. Fuller, and G.L. Pearson, *A New Silicon p-n Junction Photocell for Converting Solar Radiation into Electrical Power.* Journal of Applied Physics, 1954. **25**(5): p. 676-677.
12. Jackson, P., et al., *Properties of Cu(In,Ga)Se2 solar cells with new record efficiencies up to 21.7%.* Physica Status Solidi (RRL) – Rapid Research Letters, 2015. **9**(1): p. 28-31.
13. Rau, U. and H.W. Schock, *Chapter IC-3 - Cu(In,Ga)Se2 Thin-Film Solar Cells*, in *Practical Handbook of Photovoltaics (Second Edition)*, A. McEvoy,

T. Markvart, and L. Castañer, Editors. 2012, Academic Press: Boston. p. 323-371.

14. Wei, S.-H., S.B. Zhang, and A. Zunger, *Effects of Ga addition to CuInSe2 on its electronic, structural, and defect properties.* Applied Physics Letters, 1998. **72**(24): p. 3199-3201.
15. Markvart, T. and L. Castañer, *Chapter IA-2 - Semiconductor Materials and Modelling*, in *Practical Handbook of Photovoltaics (Second Edition)*, A. McEvoy, T. Markvart, and L. Castañer, Editors. 2012, Academic Press: Boston. p. 33-62.
16. Moller, J.H., *Semiconductor for Solar Cells*. Artech House Optoelectronics Library. 1993, Boston: Artech House Publishers.
17. Hahn, H., et al., *Untersuchungen über ternäre Chalkogenide. V. Über einige ternäre Chalkogenide mit Chalkopyritstruktur*. Zeitschrift für anorganische und allgemeine Chemie, 1953. **271**(3-4): p. 153-170.
18. Wagner, S., et al., *CuInSe2/CdS heterojunction photovoltaic detectors.* Applied Physics Letters, 1974. **25**(8): p. 434-435.
19. Mickelsen, R.A. and W.S. Chen, *High photocurrent polycrystalline thin-film CdS/CuInSe2 solar cella.* Applied Physics Letters, 1980. **36**(5): p. 371-373.
20. Devaney, W.E., et al., *Structure and properties of high efficiency ZnO/CdZnS/CuInGaSe₂ solar cells.* Electron Devices, IEEE Transactions on, 1990. **37**(2): p. 428-433.
21. Herberholz, R., et al., *Phase segregation, Cu migration and junction formation in Cu(In, Ga)Se2.* The European Physical Journal - Applied Physics, 1999. **6**(02): p. 131-139.
22. Hanna, G., et al., *Open Circuit Voltage Limitations in CuIn1–xGaxSe2 Thin-Film Solar Cells – Dependence on Alloy Composition.* Physica Status Solidi (a), 2000. **179**(1): p. R7-R8.
23. Powalla, M., et al., *Highly efficient CIS solar cells and modules made by the co-evaporation process.* Thin Solid Films, 2009. **517**(7): p. 2111-2114.
24. Razykov, T.M., et al., *Solar photovoltaic electricity: Current status and future prospects.* Solar Energy, 2011. **85**(8): p. 1580-1608.

25. Kodigala, S.R., *Chapter 2 - Growth Process of I-III-VI2 Thin Films,* in *Thin Films and Nanostructures,* K. Subba Ramaiah, Editor. 2010, Academic Press. p. 21-53.
26. Green, M. *Photovoltaics: coming of age*. in *Photovoltaic Specialists Conference, 1990., Conference Record of the Twenty First IEEE*. 1990.
27. Neamen, D.A., *Semiconductor Physics and Devices*. 1992, USA: Irwin, R.D., Inc.
28. Pierret, R.F., *Semiconductor Device Fundamentals*. 1996, USA: Addison-Wesley Publishing Company, Inc.
29. Shockley, W. and W.T. Read, *Statistics of the Recombinations of Holes and Electrons.* Physical Review, 1952. **87**(5): p. 835-842.
30. Hall, R.N., *Electron-Hole Recombination in Germanium.* Physical Review, 1952. **87**(2): p. 387-387.
31. Klenk, R., *Characterisation and modelling of chalcopyrite solar cells.* Thin Solid Films, 2001. **387**(1–2): p. 135-140.
32. Schock, H.W. and R. Scheer, *Chalcogenide Photovoltaics: Physics, Technologies, and Thin Film Devices*. 2011, Germany: Wiley-VCH.
33. Nadenau, V., et al., *Electronic properties of CuGaSe2-based heterojunction solar cells. Part I. Transport analysis.* Journal of Applied Physics, 2000. **87**(1): p. 584-593.
34. Gloeckler, M., C.R. Jenkin, and J.R. Sites. *Explanation of Light/Dark Superposition Failure in CIGS Solar Cells*. in *Compound semiconductor photovoltaics : symposium held April 22-25, 2003, San Francisco, California, U.S.A.* 2003. San Francisco, California, U.S.A.: Materials Research Society.
35. Niemegeers, A., et al., *Model for electronic transport in Cu(In,Ga)Se2 solar cells.* Progress in Photovoltaics: Research and Applications, 1998. **6**(6): p. 407-421.
36. Goldstein, J.I., et al., *Scanning Electron Microscopy and X-ray Microanalysis*. 3 ed. 2003, New York: Kluwer Academic/Plenum Publisher.
37. ASTM International, *Reference Solar Spectral Irradiance: ASTM G-173-03*. 1992, NREL: Renewable Resource Data Center.

38. Newport Corporation. *Grating Physics*. 2012 [cited 2015 20/4/2015]; Available from: http://www.newport.com/Grating-Physics/383720/1033/content.aspx.
39. Schleussner, S., et al., *Effect of gallium grading in Cu(In,Ga)Se2 solar-cell absorbers produced by multi-stage coevaporation.* Solar Energy Materials and Solar Cells, 2011. **95**(2): p. 721-726.
40. Lundberg, O., M. Edoff, and L. Stolt, *The effect of Ga-grading in CIGS thin film solar cells.* Thin Solid Films, 2005. **480–481**(0): p. 520-525.
41. Dullweber, T., et al., *Study of the effect of gallium grading in Cu(In,Ga)Se2.* Thin Solid Films, 2000. **361–362**(0): p. 478-481.

VITA

Supathat Sukaiem was born on 29th December 1989 in Surin province, Thailand. He received the Bachelor degree of Science in Physics from Chulalongkorn University in 2012.

Conference Presentation:

S. Sukaiem, B. Noikaew, B. Namnuan and S. Chatraphorn, "QUANTUM EFFICIENCY MEASUREMENTS OF CuIn1-xGaxSe2 THIN FILM SOLAR CELLS", Proceeding of the 40th Congress on Science and Technology of Thailand (STT40), 128-135, 2014.